



# Foundations of volume integral methods for eddy current problems

Mauro Passarotto\*, Silvano Pitassi, Ruben Specogna

University of Udine, Polytechnic Department of Engineering and Architecture (DPIA), EMCLab, via delle scienze 206, 33100 Udine, Italy

Received 9 July 2021; received in revised form 23 November 2021; accepted 12 January 2022

Available online xxx

## Abstract

Integral methods for solving eddy current problems use Biot–Savart law to produce non-local constitutive relations that lead to fully populated generalized mass matrices, better known as *inductance matrices*. These formulations are appealing because—unlike standard Finite Element solutions—they avoid the generation of a mesh in the insulating regions.

The aim of this paper is to alleviate the three main problems of volume integral methods. First, the computation of the inductance matrix elements is slow and also delicate because of the *singularity* in the integral equation. This paper introduces novel face basis functions that allow a much faster inductance matrix construction with respect to the standard one based on the Rao–Wilton–Glisson (RWG) or Raviart–Thomas (RT) basis functions. Second, our basis functions work for polyhedral elements formed by any number of faces (including prisms, hexahedra and pyramids), while producing the same results as RWG and RT basis functions for tetrahedral meshes.

Third, the new basis functions allow to factorize the inductance matrix and to introduce a novel family of groundbreaking low-rank inductance matrix compression techniques that show several orders of magnitude improvement in memory occupation and computational effort than state-of-the-art alternatives, allowing to solve problems that otherwise cannot be faced.

© 2022 Elsevier B.V. All rights reserved.

MSC: 78M25; 35Q61; 45E99; 65R20

Keywords: Eddy currents; Electric field integral equation; Unstructured partial equivalent electric circuit; Volume integral method; Polyhedral grid; Low-rank approximation

## 1. Introduction

Electromagnetic phenomena are governed by Maxwell's laws [1] and constitutive relations of materials. For slowly time-varying fields, whose change in magnetic field energy is dominant and electromagnetic wave propagation can be ignored, it is typical to neglect the displacement current in the Ampère–Maxwell's equation. This paper focuses on the numerical solution of these boundary value problems, referred to as eddy current problems [2]. This well-studied class of problems has a vast number of industrial applications ranging from power electronics [3,4], wireless power transfer [5], non-destructive testing and assessment of human exposure to low-frequency electromagnetic fields [6], electromagnetic breaking, metal separation in waste, induction heating [7], metal detectors and position sensing. With no purpose to be exhaustive, it can be said that various numerical methods

\* Corresponding author.

E-mail addresses: [passarotto.mauro@spes.uniud.it](mailto:passarotto.mauro@spes.uniud.it) (M. Passarotto), [pitassi.silvano@spes.uniud.it](mailto:pitassi.silvano@spes.uniud.it) (S. Pitassi), [ruben.specogna@uniud.it](mailto:ruben.specogna@uniud.it) (R. Specogna).

have been used to solve electromagnetic problems, ranging from the classical Finite Element Method (FEM) [8], Isogeometric Analysis (IGA) [9,10] and Hybridizable Discontinuous Galerkin (HDG) [11] to Mimetic Methods (MM) [12], Virtual Element Methods (VEM) [13,14] and Discrete De-Rham Methods (DDR) [15].

Other appealing techniques for solving eddy current problems are the *integral methods*—like the *Partial Element Equivalent Circuit* (PEEC) methods based on loop currents of network theory [16–20] or *Volume Integral* (VI) formulations based on the electric vector potential [21–24]. Integral methods are very appealing because, unlike the standard Finite Element differential formulations, the computational domain is formed by conductors only, so that modelling and meshing of insulators are avoided. This fact renders integral methods particularly efficient for problems involving moving conductors. Considering only conductors is made possible by formulating the eddy current problem with the *Electric Field Integral Equation* (EFIE), which uses the Biot–Savart law as a non-local constitutive relation.

However, integral methods also have two serious drawbacks. First, the discretization of the EFIE leads to a fully populated generalized mass matrix, that is called *inductance matrix* or *magnetic matrix* in the electromagnetic context. Dealing with full matrices means that the time spent for their construction and the computer memory to store them scale quadratically when the mesh is refined.<sup>1</sup> Second, the computation of an element of the inductance matrix is computationally costly since it requires the evaluation of a double integral. The double integral becomes singular for the diagonal entries of the inductance matrix, which is the manifestation of a singularity in the EFIE. The typical solution, even in recent contributions [24], is to use two different numerical integration rules for the two nested integrals. Unfortunately, as it will be shown in Section 6, this solution leads to numerical instability and to poor accuracy in the computation of the diagonal elements of the inductance matrix. For instance, as shown in Section 6, errors up to 200% may occur in the evaluation of the diagonal elements if they are computed with a double numerical integration.

The interest in integral methods revived when inductance matrix compression techniques were developed. These techniques exploit the fact that the inductance matrices have low-rank off-diagonal blocks, so that they can be approximated by using hierarchical matrices (*H*-matrices) and Adaptive Cross Approximation (ACA), see for example [20,24–27]. The compression techniques mitigate the first drawback of integral methods, providing a typical compression which ranges from 30% [27] up to 95% [24] of the total occupation of the full matrix. Yet, the time saving is very limited given that the construction of the matrix requires nearly half of the time required to compute the full matrix [24,27]. This fact limits drastically the range of problems addressable with integral methods.

To overcome the limits due to computational performances, the VoxHenry technique [4,28] has been recently introduced to solve exactly the same problem addressed in this paper. It uses the Fast Fourier Transform (FFT) to sensibly speed up the simulation, but it has the strong limitation of working with a Cartesian mesh. Such voxelized geometries present the well-known “staircase” error in the geometric representation when a slanted or curved boundary is rendered on a Cartesian grid, the same error which makes one to prefer Finite Element Method over Finite Differences. Moreover, a voxels grid prevents the use of local mesh refinement. Eventually, also Nested Equivalent Source Approximation (NESAs) techniques can be found in literature [29,30] to compress dense impedance matrices generated by surface meshes made by triangles.

This paper provides the foundations of novel compatible integral methods for solving eddy current problems that mitigate both issues of integral methods while extending the simulation speed of VoxHenry to geometrically conforming Finite Element meshes made by arbitrary polyhedra.

The state-of-the-art for tetrahedral grids is surveyed in Section 2. In particular, after recalling the standard electric field integral equation, the lowest-order Raviart–Thomas (RT) and Rao–Wilton–Glisson (RWG) face basis functions, attention is given on comparing three different techniques developed independently in literature to enforce implicitly the current conservation. It is also mentioned that another point of view of integral methods is their interpretation in terms of electrical networks, see for example [17,24]. It is remarked that this paper is deliberately focused on low-order methods for various reasons. First of all, low-order methods enable a clear circuit interpretation of the EFIE which is the main reason for the success of computer codes like FASTHENRY [17]. Second, physical and geometric parameters are generally known with a tolerance in the percent range, which means that extreme accuracy can be hardly justified for those applications. Hence, for industrial three-dimensional problems, low-order methods

<sup>1</sup> We remark that, in principle, the dominant computational effort is the solution of the full linear system whose asymptotic complexity is cubical. Yet, asymptotic complexity neglects constants: for example, for 10,000 elements, the assembly of the inductance matrix typically takes one hour whereas the system solution with a direct solver (*zsptf* and *zspts* LAPACK’s routine) just requires few seconds.

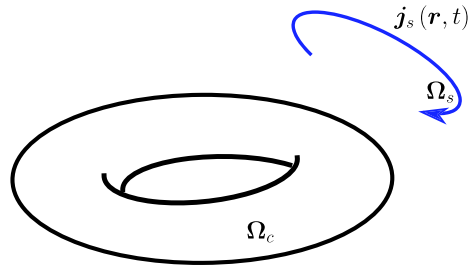


**Fig. 1.** Electromagnetic problem configuration: an arbitrarily shaped conducting body  $\Omega_c$  under the influence of the source domain  $\Omega_s$ .

that are characterized by a simpler simulation set up (e.g. high order schemes suffer from the lack of high order representation of curved geometry in off-the-shelf mesh generators) and a faster running time are more appealing in this respect.

A first contribution of this paper, developed in Section 3, is to bridge all the three methods mentioned above to enforce the current conservation showing that, while they produce the same solution in terms of current density, one of these approaches has to be preferred with respect to others in terms of computational performances.

A second contribution, shown in Section 4, discusses why it is hard to extend the volume integral method and its circuit interpretation to meshes that contain other elements than tetrahedra. It is shown that mass matrices produced with RT or RWG face basis functions for hexahedra are *not* consistent. Hence, such mass matrices cannot be generalized to arbitrary polyhedral elements.

A third contribution, contained in Section 5, is to extend the use of volume uniform face basis functions introduced in [31] for tetrahedra to volume integral formulations and general polyhedral mesh elements. They can be thought as the generalization of RWG and RT basis function for hexahedral or even general polyhedral elements because, as shown at the end of Section 5, they produce the same stiffness matrix as the RT and RWG in case of tetrahedral meshes.

The paper presents in particular two groundbreaking advantages induced by the use of the proposed basis functions. First, Section 6 shows that they enable a faster computation of the inductance matrix and, in addition, the use of a faster singularity extraction technique to compute the diagonal terms of the inductance matrix accurately; second, the novel basis functions enable an original factorization of this matrix. Then, in Section 7, the benefits of this new factorization when coupled either with low-rank compression techniques or with black box implementations of the Fast Multipole Method (FMM) [32] are exposed and compared critically to the state-of-the-art.

Finally, in Section 8, some numerical results are shown while, in Section 9, the conclusions are drawn.

## 2. State of the art EFIE to solve eddy current problems on tetrahedral grids

### 2.1. The eddy current problem: From the continuum to the discrete framework

As a physical reference framework, we consider the setting of Fig. 1, where a *conducting domain*  $\Omega_c$  of arbitrary topology—technically, a compact manifold [33] embedded in the three dimensional Euclidean space  $\Omega$ —is placed under the influence of a time-varying magnetic field. Such a source magnetic field, produced by a known current density  $\mathbf{j}_s(\mathbf{r}, t)$ —where  $\mathbf{r} \in \mathbb{R}^3$  is a point of  $\Omega$  and  $t$  a time instant—flowing in a *source domain*  $\Omega_s$ , produces an unknown induced current  $\mathbf{j}(\mathbf{r}, t)$  in  $\Omega_c$  accordingly to the Faraday–Neumann law. The conductor is characterized by its resistivity  $\rho(\mathbf{r})$  (or its reciprocal, i.e. the conductivity  $\sigma(\mathbf{r})$ ) while, for simplicity, the whole domain is considered a medium whose magnetic permeability  $\mu$  is constant in time and uniform in space and it is equal to the vacuum permeability  $\mu_0$ . In fact, the contributions introduced in this paper can be extended to problems involving magnetic materials by using consolidated techniques to deal with them like [18]. Thus, the extension of the formulation to problems containing magnetic materials is left for further developments. In the continuation, the time-and-space variation of the fields might be sometimes hidden for the sake of brevity.

We consider the total magnetic field

$$\mathbf{h}_t = \mathbf{h} + \mathbf{h}_s$$

as a sum of the unknown reaction  $\mathbf{h}(\mathbf{r}, t)$  of the conducting domain—produced by the current density  $\mathbf{j}$  in  $\Omega_c$ —with the field  $\mathbf{h}_s(\mathbf{r}, t)$  generated by  $\mathbf{j}_s$ , and the same for the total magnetic induction field

$$\mathbf{b}_t = \mathbf{b} + \mathbf{b}_s$$

in which  $\mathbf{b}(\mathbf{r}, t)$  is the unknown contribution and  $\mathbf{b}_s(\mathbf{r}, t)$  the known one produced by the current density  $\mathbf{j}_s$ .

In this framework, it is known that, under the hypothesis of magneto quasi-static approximation, the following set of equations that characterizes the sources of the problem holds in  $\Omega$

$$\nabla \cdot \mathbf{b}_s(\mathbf{r}, t) = 0, \tag{1}$$

$$\nabla \cdot \mathbf{j}_s(\mathbf{r}, t) = 0, \tag{2}$$

$$\nabla \times \mathbf{h}_s(\mathbf{r}, t) = \mathbf{j}_s(\mathbf{r}, t), \tag{3}$$

in addition the one that has to be enforced to determine the unknown eddy currents

$$\nabla \cdot \mathbf{b}(\mathbf{r}, t) = 0, \tag{4}$$

$$\nabla \cdot \mathbf{j}(\mathbf{r}, t) = 0, \tag{5}$$

$$\nabla \times \mathbf{h}(\mathbf{r}, t) = \mathbf{j}(\mathbf{r}, t), \tag{6}$$

$$\nabla \times \mathbf{e}(\mathbf{r}, t) - \frac{\partial}{\partial t} \mathbf{b}_t(\mathbf{r}, t) = \mathbf{0}. \tag{7}$$

Moreover, constitutive laws read

$$\mathbf{b}_s(\mathbf{r}, t) = \mu_0 \mathbf{h}_s(\mathbf{r}, t), \quad \mathbf{r} \in \Omega \tag{8}$$

$$\mathbf{b}_t(\mathbf{r}, t) = \mu_0 \mathbf{h}_t(\mathbf{r}, t), \quad \mathbf{r} \in \Omega \tag{9}$$

$$\mathbf{e}(\mathbf{r}, t) = \rho(\mathbf{r}) \mathbf{j}(\mathbf{r}, t), \quad \mathbf{r} \in \Omega_c \tag{10}$$

where  $\mathbf{e}(\mathbf{r}, t)$  refers to the unknown electric field related to the unknown current  $\mathbf{j}(\mathbf{r}, t)$  flowing in the conductor  $\Omega_c$ .

For the well posedness of the eddy current problem, we also consider regularity condition at infinity for  $\mathbf{h}$ ,  $\mathbf{b}$  and  $\mathbf{e}$  since  $\Omega$  is unbounded. In addition, we impose the boundary conditions on  $\mathbf{j}$  in such a way that

$$\mathbf{j}(\mathbf{r}, t) \cdot \mathbf{n} = 0, \quad \forall \mathbf{r} \in \Gamma$$

where  $\Gamma$  is the boundary of  $\Omega_c$  and  $\mathbf{n}$  is an outgoing vector normal to  $\Gamma$  in  $\mathbf{r}$ . We remark that in this paper, for the sake of simplicity in the exposition, we assume that no electrodes are present. The extension to the case with electrodes presents no difficulty and will be presented elsewhere.

Following [34], we introduce the Hilbert vector spaces  $L^2(\Omega_c)$  and  $\mathbf{L}^2(\Omega_c)$  with the usual scalar products. Then, given the subspaces  $\mathbf{H}_{\text{grad}}^1(\Omega_c) := \{\varphi \in L^2(\Omega_c) : \nabla \varphi \in \mathbf{L}^2(\Omega_c)\}$  and  $\mathbf{H}_{\text{div}}(\Omega_c) := \{\mathbf{j} \in \mathbf{L}^2(\Omega_c) : \nabla \cdot \mathbf{j} \in L^2(\Omega_c)\}$ , we define the closed subspace  $\mathbf{H}_{\text{div},0}(\Omega_c) := \{\mathbf{j} \in \mathbf{H}_{\text{div}} : \nabla \cdot \mathbf{j} = 0 \text{ in } \Omega_c, \mathbf{j} \cdot \mathbf{n} = 0 \text{ in } \Gamma\}$ . In the vector space  $\mathbf{H}_{\text{div},0}(\Omega_c)$  property  $\mathbf{H}_{\text{div},0}(\Omega_c)^\perp = \nabla \left( \mathbf{H}_{\text{grad}}^1(\Omega_c) \right)$  holds for the orthogonal subspace  $\mathbf{H}_{\text{div},0}(\Omega_c)^\perp$ . Indeed, by applying Green’s theorem we have  $\int_{\Omega_c} \nabla \phi \cdot \mathbf{j} \, dv = - \int_{\Omega_c} \phi (\nabla \cdot \mathbf{j}) \, dv + \int_\Gamma \phi (\mathbf{j} \cdot \mathbf{n}) \, dS = 0$ , where we have used the fact that vector fields  $\mathbf{j} \in \mathbf{H}_{\text{div},0}(\Omega_c)$  are solenoidal and their normal trace on  $\Gamma$  vanishes.

Because of (1) and (4), it is customary to introduce a magnetic vector potential  $\mathbf{a}_t$  so that  $\mathbf{b}_t = \nabla \times \mathbf{a}_t$  thus rewriting Faraday’s law in (7) as

$$\frac{\partial}{\partial t} \mathbf{a}_t + \mathbf{e} = -\nabla \phi \tag{11}$$

by using the electric scalar potential  $\phi$ .

In order to solve eddy currents by means of an *integral* approach, the linear integral relation called Biot–Savart law linking the magnetic vector potential on an arbitrary point of the space  $\mathbf{r} \in \Omega$  to a given current density field  $\mathbf{j}_d$  reads as

$$\mathbf{a}_d(\mathbf{r}, t) = \frac{\mu_0}{4\pi} \int_\Omega \frac{\mathbf{j}_d(\mathbf{r}', t)}{|\mathbf{r} - \mathbf{r}'|} \, dv = \mathcal{G} \mathbf{j}_d \tag{12}$$

via the integral linear operator  $\mathcal{G}$ . We note that  $\mathcal{G} \mathbf{j}_s$  gives the vector potential  $\mathbf{a}_s$  relative to the solution, in a given time instant  $t$ , of the magnetostatic problem expressed by (1), (2), (3) and (8).

By separating the known contribution  $\mathbf{a}_s$  of the source domain  $\Omega_s$  from the unknown part  $\mathbf{a}$  due the eddy currents in  $\Omega_c$ , namely  $\mathbf{a}_t = \mathbf{a} + \mathbf{a}_s$  with  $\mathbf{a} = \mathcal{G}\mathbf{j}$  and  $\mathbf{a}_s = \mathcal{G}\mathbf{j}_s$ , we obtain the Electric Field Integral Equation (EFIE) from (11) as

$$\frac{\partial}{\partial t}\mathcal{G}\mathbf{j} + \frac{\partial}{\partial t}\mathbf{a}_s + \mathbf{e} = -\nabla\phi. \tag{13}$$

To develop the finite element formulation of (13), the partial differential equations must be restated in a *weak form*, which reads

$$\frac{d}{dt}(\mathcal{G}\mathbf{j}, \mathbf{j}') + (\rho(\mathbf{r})\mathbf{j}, \mathbf{j}') = -\frac{d}{dt}(\mathbf{a}_s, \mathbf{j}'), \quad \forall \mathbf{j}' \in \mathbf{H}_{\text{div},0}(\Omega_c) \tag{14}$$

where (10) has been used and plugged into (13).

In order to solve (14) numerically, we partition the conductive domain  $\Omega_c$ , into a standard finite element mesh made by tetrahedra. The simplicial mesh  $\mathcal{K}$  will thus be formed by  $V$  volumes  $v_i$ ,  $i = 1, \dots, V$ ,  $F$  faces  $f_j$ ,  $j = 1, \dots, F$ ,  $E$  edges  $e_k$ ,  $k = 1, \dots, E$  and  $N$  nodes  $n_l$ ,  $l = 1, \dots, N$ . We assume that the generated mesh reflects the topology of the domain of interest, i.e. the mesh is adequately refined in such a way that all geometric and topological features of the domain of interest are captured. Thus, since  $\Omega_c$  is a compact manifold, the mesh  $\mathcal{K}$  is a three dimensional *combinatorial manifold with boundary* [33].

The partitioning into finite elements allows the interpolation of the current density vector field  $\mathbf{j}$  by means of suitable vector functions  $\mathbf{w}_{f_j}$  as

$$\mathbf{j}(\mathbf{r}, t) = \sum_{j=1}^F \mathbf{w}_{f_j}(\mathbf{r}) I_j(t). \tag{15}$$

The vector functions  $\mathbf{w}_{f_j}(\mathbf{r})$  are called *face basis functions* because they are attached to mesh faces. Their value, generally, depends on the position of the calculation point  $\mathbf{r}$ .  $I_j$  is the value of the current flowing through the  $j$ th face of the mesh and it configures as the degree of freedom (DoF, plural DoFs) of the discrete numerical model. The choice of the proper type of basis functions is crucial for the numerical model to be convergent, well-conditioned, robust and efficient. For this reason, we will treat this aspect separately in Section 2.2, and we now proceed without providing more accurate details how such basis functions are defined.

Eq. (14) with the use of (15) and the standard Galerkin method, which sets  $\mathbf{j}' = \mathbf{w}_f$ , yields a symmetric system of linear equations that writes

$$\mathbb{R}\mathbf{I} + \mathbb{M}\frac{d}{dt}\mathbf{I} = -\frac{d}{dt}\mathbf{A}_s, \tag{16}$$

in which the DoFs vector  $\mathbf{I}$  stores the values of the face currents  $I_j$ . Moreover, in (16), we impose the boundary conditions  $\mathbf{j}(\mathbf{r}, t) \cdot \mathbf{n} = 0$  on  $\Gamma$  by setting to zero all the DoFs  $I_j$  related to the faces that belong to the boundary of  $\mathcal{K}$ , hereafter denoted as  $\partial\mathcal{K}$ .

In order to define the other terms of the last expression, let  $\mathbb{O}^{v_h}$  be the *restriction matrix* that provides the local current DoFs of a volume  $v_h$  when it is applied to the vector  $\mathbf{I}$  of the current DoFs. Called  $F_{v_h}$  the number of local faces  $f_j^{v_h}$  of the volume  $v_h$ , forming its boundary,  $\mathbb{O}^{v_h}$  is defined as a matrix of size  $F_{v_h} \times F$  whose rows have exactly one entry equal to 1 in correspondence of the  $j$ th face  $f_j$  that belongs to the boundary of  $v_h$  and zero everywhere else.

It follows that, in a tetrahedron  $v_h$ , the  $(i, j)$  entry  $R_{ij}^{v_h}$  of the resistance matrix restricted to  $v_h$ , namely  $\mathbb{R}^{v_h}$ , where  $i = 1, \dots, F_{v_h}$  and also  $j = 1, \dots, F_{v_h}$ , results to be defined as

$$R_{ij}^{v_h} = \int_{v_h} \rho(\mathbf{r}) \mathbf{w}_{f_i}^{v_h}(\mathbf{r}) \cdot \mathbf{w}_{f_j}^{v_h}(\mathbf{r}') dv_h, \tag{17}$$

being  $\mathbf{w}_{f_i}^{v_h}(\mathbf{r})$ ,  $\mathbf{r} \in v_h$ , the basis function whose only support is the  $i$ th face of  $v_h$ . Then, by using  $\mathbb{O}^{v_h}$ , the global resistance matrix  $\mathbb{R}$  can be obtained by means of the standard finite element assembling process as

$$\mathbb{R} = \sum_{h=1}^V \mathbb{O}^{v_h T} \mathbb{R}^{v_h} \mathbb{O}^{v_h}. \tag{18}$$

In a similar way, by considering two volumes  $v_h$  and  $v_k$ , that can also be coincident, whose boundaries are composed by  $F_{v_h}$  and  $F_{v_k}$  local faces, and given the two corresponding restriction matrices  $\mathbb{O}^{v_h}$  and  $\mathbb{O}^{v_k}$ , the  $(i, j)$  entry  $M_{ij}^{v_h v_k}$  of the local inductance matrix  $\mathbb{M}^{v_h v_k}$  is first introduced as

$$M_{ij}^{v_h v_k} = \frac{\mu_0}{4\pi} \int_{v_h} \int_{v_k} \frac{\mathbf{w}_{f_i}^{v_h}(\mathbf{r}) \cdot \mathbf{w}_{f_j}^{v_k}(\mathbf{r}')}{|\mathbf{r} - \mathbf{r}'|} dv_h dv_k \tag{19}$$

from which the global one follows as

$$\mathbb{M} = \sum_{h=1}^V \sum_{k=1}^V \mathbb{O}^{v_h T} \mathbb{M}^{v_h v_k} \mathbb{O}^{v_k} \tag{20}$$

Finally, with the same reasoning, the entries of the right hand side vector  $\mathbf{A}_s$  can be computed as

$$\mathbf{A}_s = \sum_{h=1}^V \mathbb{O}^{v_h T} \mathbf{A}_s^{v_h} \tag{21}$$

in which the  $i$ th entry  $A_{s,i}^{v_h}$  of the local array  $\mathbf{A}_s^{v_h}$  is

$$A_{s,i}^{v_h} = \int_{v_h} \mathbf{a}_s(\mathbf{r}) \cdot \mathbf{w}_{f_i}^{v_h}(\mathbf{r}) dv_h \tag{22}$$

Yet, Eq. (16) alone is not sufficient since, as it is, it does not verify (5), whose discrete version on mesh  $\mathcal{K}$  reads

$$\mathbb{D}\mathbf{I} = \mathbf{0}, \tag{23}$$

where  $\mathbb{D}$  is the volumes-faces incidence matrix. In fact, a solenoidal basis for the face currents must be constructed before solving the system. To that end, in Section 2.4, we identify three different approaches followed in literature, each of them exploiting alternative techniques that, even if leading to a different set of linear systems, produce the same solution in terms of  $\mathbf{I}$ .

### 2.2. Face basis functions for tetrahedral meshes

In this section we report a brief review of how to construct the face basis functions to be used in (16). A typical requirement is to use basis functions that belong to  $\mathbf{H}_{\text{div}}$  [2,35]. As explained for instance in [35] or in [22], this imposes that the normal component of the  $\mathbf{j}$  field must be continuous through the faces of  $\mathcal{K}$ ; instead, no requirements are needed for the tangential components.

The standard choice is represented by *Whitney facet elements* better known as *Raviart–Thomas (RT) basis functions* [35,36]. They are defined starting from nodal basis functions  $\mathbf{w}_{n_i}^v(\mathbf{r})$  on a tetrahedron  $v$ , with  $n_i$  being the  $i$ th node of the considered volume. Then, the facet basis function for the  $j$ th face of a tetrahedron  $v$  is defined as

$$\mathbf{w}_{f_j}^v = 2 (\mathbf{w}_{n_a}^v \nabla \mathbf{w}_{n_b}^v \times \nabla \mathbf{w}_{n_c}^v + \mathbf{w}_{n_b}^v \nabla \mathbf{w}_{n_c}^v \times \nabla \mathbf{w}_{n_a}^v + \mathbf{w}_{n_c}^v \nabla \mathbf{w}_{n_a}^v \times \nabla \mathbf{w}_{n_b}^v), \tag{24}$$

where  $n_a, n_b$  and  $n_c$  are the boundary nodes of  $f_j$  as shown in Fig. 2a.

Another choice, which will be proved to be equivalent to RT and is popular in the computational electromagnetics community, is the use of *Rao–Wilton–Glisson (RWG) shape functions* firstly introduced for 2D simplicial elements [37] and then extended to tetrahedra [38]. Exactly as RT basis functions also RWG are *conformal*: the normal component of  $\mathbf{j}$  perfectly matches on each shared face  $f_j$  when moving from one volume to its neighbour through  $f_j$ .

Let us consider Fig. 2b wherein the face  $f_j$  is shared between two tetrahedra denoted  $T_f^+$  and  $T_f^-$ . The tetrahedra signs are chosen accordingly with the reciprocal orientation of  $f_j$  in such a way that the direction of the flux of  $\mathbf{w}_{f_j}$  has to be outgoing for  $T_f^+$  and ingoing for  $T_f^-$ , or conversely. Under this premise, the face basis function referred to  $f_j$  can be defined as

$$\mathbf{w}_{f_j}(\mathbf{r}) = \begin{cases} A_{f_j} \rho_f^+ & \text{if } \mathbf{r} \in T_f^+ \\ \frac{3|v|^+}{3|v|^+} & \\ A_{f_j} \rho_f^- & \text{if } \mathbf{r} \in T_f^- \\ \frac{3|v|^-}{3|v|^-} & \\ 0 & \text{elsewhere,} \end{cases} \tag{25}$$

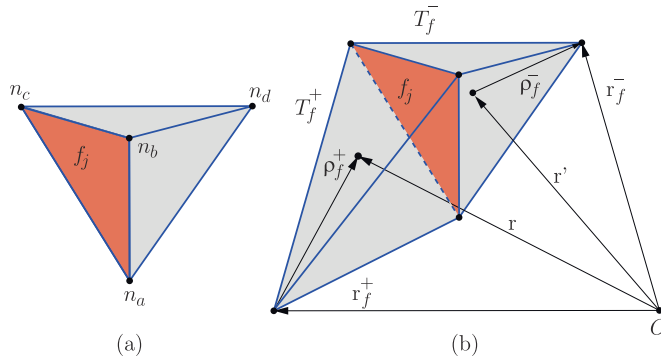


**Fig. 2.** Left: the  $j$ th face  $f_j$  whose vertices are nodes  $n_a$ ,  $n_b$ , and  $n_c$ ;  $n_d$  is the missing vertex opposite to  $f_j$ . Right: the  $j$ th face of a mesh  $\mathcal{K}$  shared between the two tetrahedra  $T_f^+$  and  $T_f^-$ .

with  $\rho_f^- := (\mathbf{r}_f^- - \mathbf{r})$ ,  $\rho_f^+ := (\mathbf{r} - \mathbf{r}_f^+)$  and where  $A_{f_j}$  is the area of  $f_j$  and  $|v|^\pm$  is the volume of  $T_f^\pm$ . Vectors  $\mathbf{r}_f^\pm$  point to the tetrahedron nodes opposite to  $f_j$  considered, respectively, either from  $T_f^+$  or from  $T_f^-$ .

It has already been shown in [39] that, even though the (24) and (25) appear to be quite different, they provide the same set of basis functions.

### 2.3. Interpretation as electrical circuits

The idea of interpreting (16) in terms of electric circuits has been already discussed in the literature but without any theoretical explanation on how this is possible. The aim of this section is to provide a rigorous interpretation of Eq. (16) in terms of electric circuits.

Let us start by showing what is the physical interpretation of the array  $\tilde{\mathbf{U}}$  in

$$\tilde{\mathbf{U}} = \mathbb{R}\mathbf{I}, \tag{26}$$

where  $\mathbf{I}$  is the vector of current DoFs and  $\mathbb{R}$  is the resistance finite element mass matrix (18). It turns out, from the study of the measurement units, that each DoF of  $\tilde{\mathbf{U}}$  is a voltage. It is therefore legitimate to ask whether there exists a path on which this voltage is sampled.

With this goal in mind, we now describe how the so-called *dual edges* are constructed. Starting from the tetrahedral mesh  $\mathcal{K}$ , it is possible to construct a *barycentric dual mesh*  $\tilde{\mathcal{K}}$  [40,41] by considering the barycenters of each volume  $v_i$  of  $\mathcal{K}$  as the *dual nodes*  $\tilde{n}_{v_i}$ ,  $i = 1, \dots, V$  of  $\tilde{\mathcal{K}}$  thus achieving the one-to-one correspondence between  $v_i$  and  $\tilde{n}_{v_i}$ . A *dual edge*  $\tilde{e}_{f_j}$ ,  $j = 1, \dots, F$  connects two dual nodes  $\tilde{n}_{v_i}$  and  $\tilde{n}_{v_h}$  passing through the barycenter of a face  $f_j$  which is shared between  $v_i$  and  $v_h$  in a one-to-one correspondence with the face  $f_j$ . Finally, a *dual face*  $\tilde{f}_{e_k}$ ,  $k = 1, \dots, E$  is in correspondence with primal edges  $e_k$  and a dual node  $\tilde{n}_{n_l}$ ,  $l = 1, \dots, N$  with primal nodes  $n_l$ . The result of this subdivision is depicted in Fig. 3.

We also define the *restriction of dual edges to a volume* as follows. Let  $v_k$  be a volume containing the face  $f_i$ . The restriction of  $\tilde{e}_{f_i}$  to  $v_k$ , denoted by  $\tilde{e}_{f_i}^{v_k}$ , is the segment connecting the dual node  $\tilde{n}_{v_k}$  with  $b_{f_i}$ , the barycenter of the face  $f_i$ . We denote by  $\tilde{\mathbf{e}}_{f_i}^{v_k}$  the edge vector associated with  $\tilde{e}_{f_i}^{v_k}$ .

Let us now consider the element-wise uniform current density

$$\mathbf{j}(\mathbf{r}) = \sum_{j=1}^F \mathbf{w}_{f_j}(\mathbf{r}) I_j \tag{27}$$

and define the element-wise uniform electric field

$$\mathbf{e}(\mathbf{r}) = \rho \mathbf{j}(\mathbf{r}). \tag{28}$$

Since also  $\mathbf{e}(\mathbf{r})$  is uniform inside each volume  $v_h$  and the following property holds, see [42],

$$\int_{v_h} \mathbf{w}_{f_i}^{v_h}(\mathbf{r}) dv_h = \tilde{\mathbf{e}}_{f_i}^{v_h} \tag{29}$$

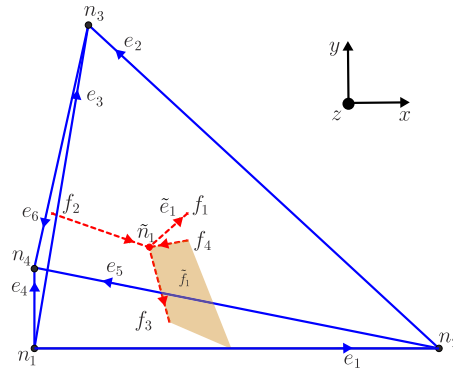


**Fig. 3.** Dual partition of a tetrahedron. Primal faces  $f_j, j = 1, \dots, 4$  are in a one-to-one correspondence with half dual edges  $\tilde{e}_{f_j}$  (dashed red lines) related to the depicted volume. (For interpretation of the references to colour in this figure legend, the reader is referred to the web version of this article.)

we have

$$\int_{v_h} \mathbf{e} \cdot \mathbf{w}_{f_i}^{v_h}(\mathbf{r}) dv_h = \mathbf{e} \cdot \int_{v_h} \mathbf{w}_{f_i}^{v_h}(\mathbf{r}) dv_h = \mathbf{e} \cdot \tilde{\mathbf{e}}_{f_i}^{v_h}. \tag{30}$$

Thus, we can finally claim that the entry  $\tilde{U}_i$  of the vector  $\tilde{\mathbf{U}}$  stores the integral of the electric field  $\mathbf{e}$  along the dual edge  $\tilde{e}_{f_i}$

$$\tilde{U}_i = \int_{\Omega} \mathbf{e}(\mathbf{r}) \cdot \mathbf{w}_{f_i}(\mathbf{r}) dv = \mathbf{e}(\mathbf{r}) \cdot (\tilde{\mathbf{e}}_{f_i}^{v_h} + \tilde{\mathbf{e}}_{f_i}^{v_k}) = \int_{\tilde{e}_{f_i}} \mathbf{e}(\mathbf{r}) \cdot d\mathbf{l}, \tag{31}$$

where  $v_h$  and  $v_k$  are the only two tetrahedra sharing the face  $f_i$ .

This geometric interpretation of the finite elements is at the root of the Discrete Geometric Approach (DGA) [43,44].

Afterwards, we move on to the physical interpretation of  $\tilde{\mathbf{A}} = \mathbb{M}\mathbf{I}$ . It turns out, from the study of measurement units, that the time derivative of each DoF of  $\tilde{\mathbf{A}}$  is a voltage. Thus, in analogy to what was done before, we ask ourselves if there exists a path on which this voltage is sampled. To this end, let us consider the vector field

$$\mathbf{a}(\mathbf{r}) = \frac{\mu_0}{4\pi} \int_{\Omega} \frac{\mathbf{j}(\mathbf{r}')}{|\mathbf{r} - \mathbf{r}'|} dv. \tag{32}$$

where  $\mathbf{j}$  is defined as in (27). Yet, contrary to the previous case, the  $i$ th entry of  $\tilde{\mathbf{A}}$ , namely  $\tilde{A}_i$ , cannot be directly interpreted as the line integral of the magnetic vector potential on dual edges. Indeed, we have that

$$\tilde{A}_i = \int_{\Omega} \mathbf{a}(\mathbf{r}) \cdot \mathbf{w}_{f_i}(\mathbf{r}) dv \tag{33}$$

is in general different from

$$\int_{\tilde{e}_{f_i}} \mathbf{a}(\mathbf{r}) \cdot d\mathbf{l}. \tag{34}$$

To get an interpretation of  $\tilde{\mathbf{A}}$  as the line integral of the magnetic vector potential on dual edges, we introduce the element-wise uniform vector field

$$\mathbf{a}_m(\mathbf{r}) = \frac{1}{|v_h|} \int_{v_h} \mathbf{a}(\mathbf{r}) dv_h, \mathbf{r} \in v_h, \tag{35}$$

namely the average vector field of  $\mathbf{a}(\mathbf{r})$  on each volume  $v_h$ . Since  $\mathbf{a}_m(\mathbf{r})$  is element-wise uniform we clearly have

$$\int_{v_h} \mathbf{a}_m \cdot \mathbf{w}_{f_i}^{v_h}(\mathbf{r}) dv_h = \mathbf{a}_m \cdot \int_{v_h} \mathbf{w}_{f_i}^{v_h}(\mathbf{r}) dv_h = \mathbf{a}_m \cdot \tilde{\mathbf{e}}_{f_i}^{v_h}. \tag{36}$$

so that (33) can be recast as

$$A_{m,i} = \int_{\Omega} \mathbf{a}_m(\mathbf{r}) \cdot \mathbf{w}_{f_i}(\mathbf{r}) dv = \mathbf{a}_m(\mathbf{r}) \cdot \left( \tilde{\mathbf{e}}_{f_i}^{v_h} + \tilde{\mathbf{e}}_{f_i}^{v_k} \right) = \int_{\tilde{e}_{f_i}} \mathbf{a}_m(\mathbf{r}) \cdot d\mathbf{l}, \quad (37)$$

where, as before,  $v_h$  and  $v_k$  are the only two tetrahedra sharing the face  $f_i$ .

We now prove that the difference between  $A_{m,i}$  and  $\tilde{A}_i$  exhibits a faster convergence order than the discretization error when the mesh is refined. Thus, the approximation made in replacing  $\mathbf{a}(\mathbf{r})$  with  $\mathbf{a}_m(\mathbf{r})$  is negligible in practice and yet it allows to formally introduce a network interpretation of the physical quantities. Let us consider the difference on a single volume  $v_h$

$$\int_{v_h} (\mathbf{a}(\mathbf{r}) - \mathbf{a}_m) \cdot \mathbf{w}_{f_i}^{v_h}(\mathbf{r}) dv_h = \frac{\tilde{\mathbf{e}}_{f_i}^{v_h}}{|v_h|} \cdot \int_{v_h} (\mathbf{a}(\mathbf{r}) - \mathbf{a}_m) dv_h + \int_{v_h} (\mathbf{a}(\mathbf{r}) - \mathbf{a}_m) \cdot \left( \mathbf{w}_{f_i}^{v_h}(\mathbf{r}) - \frac{\tilde{\mathbf{e}}_{f_i}^{v_h}}{|v_h|} \right) dv_h. \quad (38)$$

First, note that  $\int_{v_h} (\mathbf{a}(\mathbf{r}) - \mathbf{a}_m) dv_h$  is zero because of the definition of  $\mathbf{a}_m$ . Second,  $(\mathbf{a}(\mathbf{r}) - \mathbf{a}_m)$  and  $(\mathbf{w}_{f_i}^{v_h}(\mathbf{r}) - \frac{\tilde{\mathbf{e}}_{f_i}^{v_h}}{|v_h|})$  are at least linear fields with zero average so that  $|A_{s,i} - \tilde{A}_i|$  exhibits a second convergence order with respect to the mesh size.

Only now that we know that a path on which voltages are defined exists, we can interpret the discretized EFIE (16) with an electric circuit that can be solved by standard methods of *network analysis*. The graph of the electrical network is thus formed by dual nodes and dual edges of  $\mathcal{K}$ . We remark that, because of boundary conditions, the dual edges which are dual to faces in  $\partial\mathcal{K}$  do not belong to the dual graph.

Thanks to this interpretation, the left hand side of Eq. (16) can be regarded as the resistive and inductive voltage drop caused by the current flow. This, in the frequency domain, configures  $\mathbb{R} + i\omega\mathbb{M}$  as the impedance of  $\Omega_c$  which writes

$$\mathbb{Z}\mathbf{I} = -i\omega\tilde{\mathbf{A}}_s \quad (39)$$

being  $\omega = 2\pi f$  the angular frequency and  $i$  the imaginary unit.

## 2.4. Solenoidal currents

We now deal with the issue of enforcing implicitly (23) on  $\mathcal{K}$ . As announced, we compare three different approaches followed in literature that will be shown to be strictly related.

### 2.4.1. Solution based on the electric vector potential and additional DoFs: The CARIDDI code

Historically, a first solution was proposed in 1985 by Albanese and Rubinacci [45]. They had the idea of representing the solenoidal current density as the curl of an *electric vector potential*  $\mathbf{t}$

$$\mathbf{j}(\mathbf{r}, t) = \nabla \times \mathbf{t}(\mathbf{r}, t). \quad (40)$$

In the discrete setting, the current density is represented inside the tetrahedron  $v$  by

$$\mathbf{j}(\mathbf{r}, t) = \sum_{k=1}^6 \nabla \times N_{e_k}^v(\mathbf{r}) T_k(t), \quad (41)$$

where  $N_{e_k}^v$  are the *Nédélec's edge basis functions* [46] defined inside element  $v$  and  $T_k(t)$  is the line integral of  $\mathbf{t}$  on the  $k$ th edge of  $v$ . This gives rise to the system of equations

$$\mathbb{R}^{CAR}\mathbf{T} + \mathbb{L}^{CAR} \frac{d}{dt} \mathbf{T} = -\frac{d}{dt} \mathbf{U}^{CAR} \quad (42)$$

in which, following the discussion in [22], we have that

- the  $(i, j)$  entry of  $\mathbb{R}^{CAR}$  is

$$R_{ij}^{CAR} = \int_{v_h} \rho(\mathbf{r}) \nabla \times N_{e_i}^{v_h}(\mathbf{r}) \cdot \nabla \times N_{e_j}^{v_h}(\mathbf{r}') dv, \quad \forall h \in \{1, \dots, V\} \quad (43)$$

- the  $(i, j)$  entry of  $\mathbb{L}^{CAR}$  is

$$L_{ij}^{CAR} = \frac{\mu_0}{4\pi} \int_{v_h} \int_{v_k} \frac{\nabla \times \mathbf{N}_{e_i}^{v_h}(\mathbf{r}) \cdot \nabla \times \mathbf{N}_{e_j}^{v_k}(\mathbf{r}')}{|\mathbf{r} - \mathbf{r}'|} dv_h dv_k, \quad \forall h, k \in \{1, \dots, V\}; \quad (44)$$

- the  $i$ th entry of the right hand side is

$$U_i^{CAR} = \int_{v_h} \mathbf{a}_s \cdot \nabla \times \mathbf{N}_{e_i}^{v_h}(\mathbf{r}) dv, \quad \forall h \in \{1, \dots, V\}. \quad (45)$$

The unknown vector  $\mathbf{T}$  of DoFs contains line integrals of  $\mathbf{t}$  on all mesh edges. To reduce the unknowns and obtain a full rank system, the so-called *tree-cotree gauge* [21] was developed, which foresees setting to zero the entries of the array  $\mathbf{T}$  on a suitable spanning tree of  $\mathcal{K}$ . More details of gauging will be provided in Section 3.

It is fundamental to note that (42) holds only for simply connected conductors. The most up-to-date extension to conductors that are not simply connected is presented in [47] and it is based on adding some “additional DoFs”. These additional DoFs do not have a precise mathematical definition, therefore the approach lacks clear theoretical foundations. More importantly, an efficient way to find the global basis functions is missing. With the approach proposed in [47], the computation of such global basis functions may easily take hours given that it requires the solution of many global linear systems.

#### 2.4.2. Solution based on mesh current analysis (MCA): The unstructured partial elements equivalent circuit (PEEC) for eddy currents

A second approach exploits the electric circuits interpretation and solves the problem by applying the *mesh current analysis* (MCA), which is a standard method of network theory [48,49]. This approach, proposed for the first time as far as we know in [17], computes a cycle basis on the circuit graph with the help of a tree-cotree decomposition. In particular, once one adds a cotree dual edge to the tree of the dual graph, exactly one loop is created. The set of these loops built for all cotree edges forms a cycle basis of the graph [48,49]. These *global cycles* may be interpreted on the primal complex as a set of faces which produce a basis for solenoidal currents. Greater details are provided in Section 3. This approach has been recently rediscovered and called *unstructured* Partial Elements Equivalent Circuit (PEEC) for eddy currents, see for example [50].

#### 2.4.3. Solution based on algebraic topology: the VINCO code

The third possible solution, introduced in [51], stems from the discrete design of the potentials with the help of algebraic topology [40]. In this case, the so-called *cohomology theory* tells us formally—by its very definition—that all solenoidal currents  $\mathbf{I}$  (formally, a 2-cocycle [40]) can be spanned by

$$\mathbf{I} = \mathbb{C}\mathbf{T} + \mathbb{W}\mathbf{i}, \quad (46)$$

where the DoFs array  $\mathbf{T}$  stores the integral of the electric vector potential on mesh edges (formally, a 1-cochain),  $\mathbf{i}$  the array of *independent currents* [51,52] and the columns of  $\mathbb{W}$  store the representatives of generators of the *second relative cohomology group*  $H^2(\mathcal{K}, \partial\mathcal{K})$  [40], see Fig. 4a.

Cohomology theory may seem scary at first, but it has a clear physical meaning and it is unavoidable to develop a general solution. Looking at (46), the second relative cohomology group  $H^2(\mathcal{K}, \partial\mathcal{K})$ , by its very definition, spans solenoidal fields tangent to  $\partial\mathcal{K}$  that are not curl of anything. As an example, the  $\mathbb{W}$  for a solid toric conductor is formed by a single column whose entries, interpreted as electric current DoFs, form a unit current that flows through the red thin tube around the torus, see Fig. 4a. The independent currents  $\mathbf{i}$  are additional unknowns of the eddy current problem. Their number is usually very small since it depends on the topology of the conductor, in particular its number of “handles”. We also note that the dual of the faces in the red thin tube form a dual cycle made by dual edges that goes around the torus like in Fig. 4b.

A second advantage of using cohomology theory is that there exist efficient algorithms for the automatic computation of  $\mathbb{W}$ . For efficiency, it is preferable to construct  $\mathbb{W}$  by working on  $\partial\mathcal{K}$  only, first because there are less geometric elements to process in  $\partial\mathcal{K}$  than in  $\mathcal{K}$ . Second, the algorithms are intrinsically simpler and they exhibit a linear complexity in the worst case. As shown in [52],  $\mathbb{W}$  may be constructed starting from elements of the boundary as  $\mathbb{W} = \mathbb{C}\mathbb{H}$ , where columns of matrix  $\mathbb{H}$  store some suitable representative of the *first cohomology group*  $H^1(\partial\mathcal{K})$  [40] generator. In case of the example, the representatives  $\mathbf{c}^1$  and  $\mathbf{c}^2$  of the two boundary generators

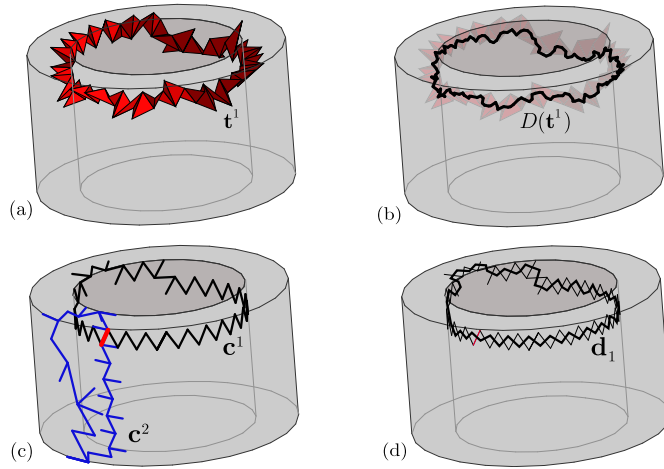


**Fig. 4.** Examples of cohomology generators  $H^2(\mathcal{K}, \partial\mathcal{K})$  and  $H^1(\partial\mathcal{K})$  for a solid torus. a) The support of a representative  $\mathbf{t}^1 \in H^2(\mathcal{K}, \partial\mathcal{K})$  generator. b) The dual of  $\mathbf{t}^1$  is a cycle made of dual edges that are dual to the faces of  $\mathbf{t}^1$ . (c) The support of two representatives  $\mathbf{c}^1, \mathbf{c}^2$  of the  $H^1(\partial\mathcal{K})$  generators of  $\partial\mathcal{K}$ . (d) The support of the homology generator  $\mathbf{d}_1 = D(\mathbf{c}^1)$  is constituted by dual edges that are dual to the primal edges of  $\mathbf{c}^1$ .

for a torus are shown in Fig. 4c; they are stored into the column of  $\mathbb{H}$ . In this case,  $\mathbf{t}^1$  can be obtained as  $\mathbb{C}\mathbf{c}^1$ . Moreover, the dual  $\mathbf{d}_1 = D(\mathbf{c}^1)$  of  $\mathbf{c}^1$ , shown in Fig. 4d, is a dual cycle homologous to  $D(\mathbf{t}^1)$ , where  $D$  denotes the duality map.

Yet, there is also a theoretical downside of using  $\partial\mathcal{K}$  only: the major difficulty here is that the  $H^1(\partial\mathcal{K})$  cohomology group produces twice the number of generators of a  $H^2(\mathcal{K}, \partial\mathcal{K})$  basis. For example, when dealing with the solid torus depicted in Fig. 4, the two boundary generators able to represent the poloidal and toroidal currents that flow in  $\partial\mathcal{K}$  appear. A first solution proposed in [51,52] suggests to use all representatives of the  $H^1(\partial\mathcal{K})$  basis to produce the  $\mathbb{W}$  matrix by pre-multiplying the representative by the  $\mathbb{C}$  matrix. The obtained  $\mathbb{W}$  is called a *lazy cohomology basis* and the obtained system turns out to be singular. Yet, most iterative and direct solvers do not have any problem in solving it since it is algebraically consistent. On the contrary, if one wants for some reason to obtain a full rank system, a cheap technique to find the required change of cohomology basis to obtain the matrix  $\mathbb{H}$  has been introduced in [52] and described in more detail in [24]. Consequently, by using  $\mathbb{W} = \mathbb{C}\mathbb{H}$ , the current is thus represented with

$$\mathbf{I} = \mathbb{C}(\mathbf{T} + \mathbb{H}\mathbf{i}). \tag{47}$$

By enforcing the discrete Faraday’s law locally on the boundary of all dual faces as  $\mathbb{C}^T \tilde{\mathbf{U}} + i\omega \mathbb{C}^T (\tilde{\mathbf{A}} + \tilde{\mathbf{A}}_s) = \mathbf{0}$  and globally on the non-local dual cycles like  $D(\mathbf{t}^1) = D(\mathbb{C}\mathbf{c}^1)$  of Fig. 4b as  $\mathbb{H}^T (\mathbb{C}^T \tilde{\mathbf{U}} + i\omega \mathbb{C}^T (\tilde{\mathbf{A}} + \tilde{\mathbf{A}}_s)) = \mathbf{0}$ , the complete set of equations reads as

$$\begin{bmatrix} \mathbb{K} & \mathbb{K}\mathbb{H} \\ \mathbb{H}^T \mathbb{K} & \mathbb{H}^T \mathbb{K}\mathbb{H} \end{bmatrix} \begin{bmatrix} \mathbf{T} \\ \mathbf{i} \end{bmatrix} = \begin{bmatrix} -i\omega \mathbb{C}^T \tilde{\mathbf{A}}_s \\ -i\omega \mathbb{H}^T \mathbb{C}^T \tilde{\mathbf{A}}_s \end{bmatrix}, \tag{48}$$

where

$$\mathbb{K} = \mathbb{C}^T (\mathbb{R} + i\omega \mathbb{M}) \mathbb{C}. \tag{49}$$

Exactly like in CARIDDI, we set to zero the entries of the array  $\mathbf{T}$  relative to edges on  $\partial\mathcal{K}$  because of boundary conditions and, to reduce the unknowns and obtain a full rank system, one may apply the *tree-cotree gauge* [21] by setting to zero the entries of the array  $\mathbf{T}$  on a suitable tree inside  $\mathcal{K}$ .

#### 2.4.4. Which solution is the best?

Even if developed independently in the literature, next section shows the relationship between all these three methods. It will be shown that all three methods return the same solution up to machine precision or linear solver

algebraic error because they are algebraically equivalent (i.e. they enforce equivalent constraints). Nevertheless, even if they are identical concerning accuracy of the solution, they are *not* in terms of computational efficiency especially when applied to large problems that requires advanced compression algorithms.

### 3. Bridging all volumetric integral methods for solving eddy currents

The easiest method to introduce the EFIE for eddy currents is the one based on MCA, known also as unstructured PEEC for eddy currents, because all topological issues are seamlessly taken into account<sup>2</sup> when computing the cycle basis of the dual graph. Yet, as a downside, there is no control on the length of the cycle basis. In practice each cycle runs through a large portion of the mesh. This fact has terrible consequences, given that state-of-the-art system matrix compression techniques do not work at all on matrices produced with such a cycle basis.

It is therefore natural to ask if there are techniques to find the *shortest cycle basis* or at least one of its close approximations. *Shortest* in our case means a basis with the minimum number of total dual edges contained in all the cycles. This is not directly feasible with graph theoretic algorithms, since the complexity of general algorithms to compute a minimal cycle basis is cubical in the number of graph edges. Therefore, a practical solution has to exploit some additional structure of the problem.

#### 3.1. VINCO is a MCA method with a short cycle basis

The main idea is that the boundary of a dual face is a “short” dual cycle and we can try to build a cycle basis from the *local cycles* produced by taking the boundaries of all dual faces. What is missing is just a recipe to extract a set of local cycles in such a way they form a basis.

How many independent local loops one has to add? To answer this question we note that, thanks to Stokes’ theorem, local cycles are dependent if their dual faces form a closed surface. Therefore, we have to avoid closed surfaces in the set of dual faces. This can be realized by removing the local cycles relative to dual faces that are dual to a primal edges which belong to a suitable spanning tree of  $\mathcal{K}$ .

There is another issue. When the topology is not trivial, local loops alone are not able to span all the cycle basis. By definition of homology, what is needed in addition is a  $H_1(\tilde{\mathcal{K}})$  homology basis. The representatives of this homology basis are called *global dual cycles* and they are obtained as the dual of the cohomology generators. For example, the global dual cycle in Fig. 4b is obtained by  $D(\mathbf{t}^1)$  or by  $D(\mathbb{C}\mathbf{c}^1)$ .

What follows is a formal proof of the claim of this section. We show in particular that the rank of the cycle basis obtained by VINCO is the same as the one obtained by the MCA method. We start from the Euler–Poincaré formula for combinatorial 3-manifolds

$$N - E + F - V = \beta_0(\mathcal{K}) - \beta_1(\mathcal{K}) + \beta_2(\mathcal{K}), \quad (50)$$

where  $\beta_i(\mathcal{K})$  is the *i*th Betti number [40] of the polyhedral grid  $\mathcal{K}$ . We write also the Euler–Poincaré formula for combinatorial 2-manifolds like the boundary of  $\mathcal{K}$ :

$$N^b - E^b + F^b = \beta_0(\partial\mathcal{K}) - \beta_1(\partial\mathcal{K}) + \beta_2(\partial\mathcal{K}), \quad (51)$$

where  $N^b$ ,  $E^b$  and  $F^b$  are the number of nodes, edges and faces contained in  $\partial\mathcal{K}$ , respectively. We remark that in the considered case  $\partial\mathcal{K}$  is a surface without boundary. A more general setting will be considered in a forthcoming work.

Here we find how many cycles are contained inside the cycle basis of the MCA method. Considering the boundary conditions, the number  $c_{MCA}$  of internal loop currents is

$$c_{MCA} = (F - F^b) - V + \beta_0(\mathcal{K}), \quad (52)$$

since the edges of the tree are number of available dual edges minus dual nodes plus the number of connected components.

From 50 we have that

$$F - V = \beta_0(\mathcal{K}) - \beta_1(\mathcal{K}) + \beta_2(\mathcal{K}) + E - N \quad (53)$$

<sup>2</sup> Actually, the computation of the cycle basis on the dual graph  $\tilde{\mathcal{G}}$  is exactly the computation of the generators of the  $H_1(\tilde{\mathcal{G}}, \mathbb{Z})$  homology group [53, p. 506].

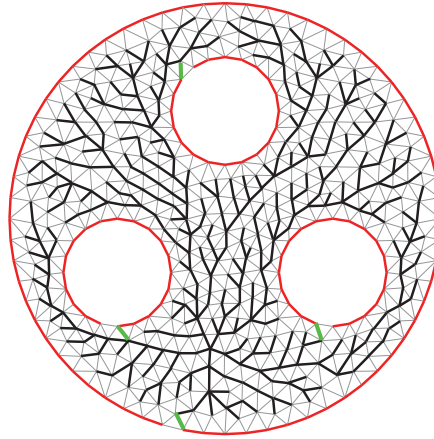


**Fig. 5.** An example of a spanning tree suitable for gauging. The example represents a two-dimensional domain for clarity. Dark black edges form an internal tree, whereas thick red edges form a tree on  $\partial\mathcal{K}$ . Thick green edges transform a forest in a spanning tree of  $\mathcal{K}$ . (For interpretation of the references to colour in this figure legend, the reader is referred to the web version of this article.)

and

$$F^b = \beta_0(\partial\mathcal{K}) - \beta_1(\partial\mathcal{K}) + \beta_2(\partial\mathcal{K}) + E^b - N^b. \tag{54}$$

Let us substitute these two (53) and (54) inside (52) to get

$$c_{MCA} = [\beta_0(\mathcal{K}) - \beta_1(\mathcal{K}) + \beta_2(\mathcal{K}) + E - N] + \beta_0(\mathcal{K}) - [\beta_0(\partial\mathcal{K}) - \beta_1(\partial\mathcal{K}) + \beta_2(\partial\mathcal{K}) + E^b - N^b]. \tag{55}$$

Let us rearrange the terms as

$$c_{MCA} = E - N + \beta_0(\mathcal{K}) + [\beta_0(\mathcal{K}) - \beta_0(\partial\mathcal{K})] - [\beta_1(\mathcal{K}) - \beta_1(\partial\mathcal{K})] + [\beta_2(\mathcal{K}) - \beta_2(\partial\mathcal{K})] - [E^b - N^b]. \tag{56}$$

Let us use the relationship between Betti numbers to simplify the last formula. Let us call  $\beta_0(\mathcal{K}) = c$  the number of connected components of  $\mathcal{K}$ . Let us call  $\beta_1(\mathcal{K}) = g$ , where  $g$  is the *genus* of  $\mathcal{K}$ . Then, it is well known that  $\beta_1(\partial\mathcal{K}) = 2g$ . Let us call  $\beta_2(\mathcal{K}) = p$ , where  $p$  is the number of *cavities* (or *voids*) of  $\mathcal{K}$ . Then, the number of connected components  $\beta_0(\partial\mathcal{K})$  of  $\partial\mathcal{K}$  is  $\beta_0(\partial\mathcal{K}) = p + c$ . Concerning the number  $\beta_2(\partial\mathcal{K})$  of cavities of  $\partial\mathcal{K}$ , they are  $p + c$ . Finally,  $\beta_3(\mathcal{K}) = 0$ . By substituting these results we have

$$\begin{aligned} & \beta_0(\mathcal{K}) + [\beta_0(\mathcal{K}) - \beta_0(\partial\mathcal{K})] - [\beta_1(\mathcal{K}) - \beta_1(\partial\mathcal{K})] + [\beta_2(\mathcal{K}) - \beta_2(\partial\mathcal{K})] \\ &= c + [c - p - c] - [g - 2g] + [p - c - p] \\ &= g - p. \end{aligned} \tag{57}$$

By substituting this result inside (56) we get

$$c_{MCA} = E - N + g - p - [E^b - N^b]. \tag{58}$$

Let us now compute the number  $c_{VI}$  loop currents produced by the VINCO framework and show that they are the same as  $c_{MCA}$ . The primal tree produced by taking into account the gauging constraints contains the following number of edges

$$(N - N^b) - c + N^b - (p + c) + p + c = N - c, \tag{59}$$

where  $(N - N^b) - c$  is the number of edges of an internal tree (i.e. a tree made by using the mesh edges and nodes in  $\mathcal{K} \setminus \partial\mathcal{K}$ ),  $N^b - (p + c)$  the boundary tree (i.e. a tree made by using the mesh edges and nodes in  $\partial\mathcal{K}$ ). To get a spanning tree of  $\mathcal{K}$ ,  $p + c$  edges have to be added, see Fig. 5. We remark that this is the same number of edges of any unconstrained tree of  $\mathcal{K}$ . The constraint is needed just to being able to enforce boundary conditions. Therefore,

the unknowns of the VINCO formulation are internal cotree edges (on the boundary they are set to zero because of boundary conditions) plus  $g$  cohomology generators

$$\begin{aligned} c_{VI} &= E - E^b - [(N - N^b) - c + p + c] + g \\ &= c_{MCA}, \end{aligned} \tag{60}$$

since the obtained expression is exactly Eq. (58).

To conclude, we can state that the VINCO is able to obtain a quasi-minimal cycle basis. There exist techniques also to minimize the global loops which result from cohomology when the domain is not simply connected, see for example [24], but, in the authors' opinion, usually there is no sensible gain in doing it in our setting.

We also remark that in general it is also interesting to use an *ungauged* formulation<sup>3</sup>, lazy cohomology generators or both. We will explore also these solutions in the numerical results section.

### 3.2. CARIDDI is a particular case of VINCO

The equivalence between CARIDDI and VINCO in case of a simply-connected conductor could be soon established by using the results of [54]. By applying them, we get

$$\mathbb{K} = \mathbb{C}^T (\mathbb{R} + i\omega\mathbb{M}) \mathbb{C} = \mathbb{C}^T \mathbb{R}\mathbb{C} + i\omega\mathbb{C}^T \mathbb{M}\mathbb{C} = \mathbb{R}^{CAR} + i\omega\mathbb{L}^{CAR}. \tag{61}$$

Thus, all the results on cohomology computation obtained in VINCO can be directly applied to CARIDDI.

To summarize, all three methods differ just in the dual cycles bases used, therefore they can be thought as equivalent from the theoretical point of view and their solutions are the same. Concerning the computational efficiency, VINCO has been already demonstrated faster than the alternatives. In Section 7 these advantages are much improved and pushed to the limits.

## 4. Generalization to hexahedral and polyhedral meshes

The aim of this section is to show that extending the integral method on hexahedral or general polyhedral meshes is not trivial. A first indication is that the circuit interpretation of CARIDDI and PEEC methods on hexahedral meshes by using standard Raviart–Thomas face basis functions [55] lacks theoretical foundations.

We start by claiming that the Raviart–Thomas mass matrix on a hexahedron is *not consistent*. Let the coordinates of the nodes of the hexahedron  $v$  in Fig. 6a be as in the caption of the picture. We assume a unitary uniform resistivity. We denote with  $p_{f_i}$ , with  $i = 1, \dots, F_v$  the intersection between face  $f_i$  and the corresponding dual edge  $\tilde{e}_{f_i}^v$ . Let  $\tilde{n}_v$  be the dual node in  $v$ . We stress that, for the present discussion, the points  $p_{f_i}$  and  $\tilde{n}_v$  are arbitrary positions and do not necessarily coincide with the barycenter of face  $f_i$  and hexahedron  $v$ , respectively. A necessary and sufficient condition for the consistency of  $\mathbb{R}^v$  according to the definition reported in [42,44] is

$$\mathbb{R}^v \mathbb{F}^v = \tilde{\mathbb{E}}^{vT}, \tag{62}$$

where  $\mathbb{F}^v$  and  $\tilde{\mathbb{E}}^v$  are, respectively, the  $F_v \times 3$  and  $3 \times F_v$  matrices in which, for  $\mathbb{F}^v$ , the  $i$ th row represents the three components of the face vector  $\mathbf{f}_i$  and for  $\tilde{\mathbb{E}}^v$  its  $i$ th column corresponds to the dual edge vector  $\tilde{e}_{f_i}^v$  restricted to  $v$ , with  $i = 1, \dots, F_v$ . In what follows we will prove that condition (62) is *not* satisfied for *any* choice of the dual grid. By direct computation, the right hand side of (62) yields

$$\begin{aligned} \text{row}_i(\mathbb{R}^v \mathbb{F}^v) &= (0, 0, 3 \log(2)/4), & \text{with } i = 1, 2 \\ \text{row}_i(\mathbb{R}^v \mathbb{F}^v) &= (3/4, 0, 0), & \text{with } i = 3, 4 \\ \text{row}_i(\mathbb{R}^v \mathbb{F}^v) &= (-1/4, 1/2, 0), & \text{with } i = 5, 6, \end{aligned}$$

where with  $\text{row}_i$  we denote the  $i$ th row of an array. Let us consider the vectors  $\tilde{e}_{f_1}^v, \tilde{e}_{f_2}^v$  associated with the dual edges  $\tilde{e}_{f_1}^v, \tilde{e}_{f_2}^v$  respectively; in order to guarantee that  $\tilde{e}_{f_1}^v, \tilde{e}_{f_2}^v$  are parallel to the vectors  $\text{row}_i(\mathbb{R}^v \mathbb{F}^v) = (0, 0, 3 \log(2)/4)$ , with  $i = 1, 2$ , it is necessary that  $\tilde{n}_v, p_{f_1}$  and  $p_{f_2}$  are on a straight line parallel to the  $z$ -axis of the Cartesian

<sup>3</sup> The ungauged formulation is the formulation as exposed in Section 2.4.3 in which the tree-cotree gauge is not applied thus producing an underdetermined system of equations.

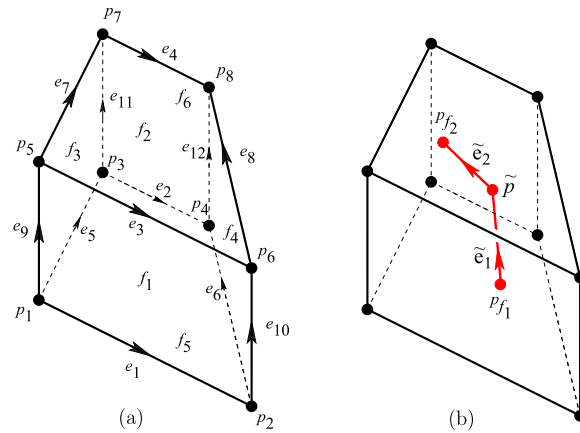


**Fig. 6.** The hexahedron  $v$  used in the counterexample. The coordinates of the nodes are  $p_1 = (0, 0, 0)$ ,  $p_2 = (2, 0, 0)$ ,  $p_3 = (0, 1, 0)$ ,  $p_4 = (1, 1, 0)$ ,  $p_5 = (0, 0, 1)$ ,  $p_6 = (2, 0, 1)$ ,  $p_7 = (0, 1, 1)$ ,  $p_8 = (1, 1, 1)$ .

coordinate system. Thus, by assuming for  $\tilde{\mathbf{n}}_v = (x_2, y_2, x_2)$  it results in  $\mathbf{p}_{f_1} = (x_2, y_2, 0)$ ,  $\mathbf{p}_{f_2} = (x_2, y_2, 1)$ . Then, given that  $\hat{\mathbf{z}}$  is the unitary vector  $(0, 0, 1)$ , it is

$$\begin{aligned} \frac{3}{2} \log(2) &= (\text{row}_1(\mathbb{R}^v \mathbb{F}^v) + \text{row}_2(\mathbb{R}^v \mathbb{F}^v)) \cdot \hat{\mathbf{z}} = \\ (\tilde{\mathbf{e}}_{f_1}^v + \tilde{\mathbf{e}}_{f_2}^v) \cdot \hat{\mathbf{z}} &= ((\tilde{\mathbf{n}}_v - \mathbf{p}_{f_1}) + (\mathbf{p}_{f_2} - \tilde{\mathbf{n}}_v)) \cdot \hat{\mathbf{z}} = \\ ((0, 0, x_2) + (0, 0, 1 - x_2)) \cdot \hat{\mathbf{z}} &= 1 \end{aligned}$$

which is clearly false.

A consequence of the fact that consistency condition (62) does *not* hold is that the voltages  $\tilde{\mathbf{U}}$  obtained by

$$\tilde{\mathbf{U}} = \mathbb{R}_{\text{RT}}^v \mathbf{I}, \tag{63}$$

where  $\mathbb{R}_{\text{RT}}$  is the Raviart–Thomas resistance mass matrix and  $\mathbf{I}$  is a set of solenoidal currents on the faces of  $v$  corresponding to a uniform current density, cannot exist, i.e. there exists no segment on which  $\tilde{\mathbf{U}}$  can be evaluated. This, in our opinion, renders the interpretation in terms of circuits questionable whenever applied to an hexahedral mesh whose constitutive matrices are computed by means of Raviart–Thomas shape functions.

To generalize in a consistent way the integral formulations for eddy currents to hexahedral meshes and even the most general polyhedral meshes we need to use the VINCO framework. This framework not only allows to obtain a consistent matrix on a mesh constituted by arbitrary polyhedra but it also enables to present the novel and original results contained in the next sections.

### 5. Novel construction of mass matrices

In this section we introduce novel basis functions which are uniform inside polyhedral elements. They are a key ingredient to produce mass matrices and generalized mass matrices that are positive-definite, symmetric and consistent for arbitrary polyhedral elements. This property has strong implications from both a theoretical and a practical point of view that will be analysed in the forthcoming sections.

#### 5.1. Volume uniform (VU) face basis functions

**Lemma 1.** Let  $\mathbf{j}$  be a constant vector field defined on a volume  $v_h$ . Define  $\tilde{\mathbf{e}}_f^{v_h} := \mathbf{b}_f - \tilde{\mathbf{n}}_{v_h}$  with  $\mathbf{b}_f$  the barycenter of a face  $f$  of  $v_h$ . The following equality holds

$$\mathbf{j} = \frac{1}{|v_h|} \sum_{f \in \partial v_h} \tilde{\mathbf{e}}_f^{v_h} I_f. \tag{64}$$

**Proof.** Let  $\mathbf{w}, \mathbf{x} \in \mathbb{R}^3$ . Let  $\mathbf{n}_{\partial v_h}$  denote the outgoing vector normal to  $\partial v_h$ . We have

$$|v_h| \mathbf{j} \cdot \mathbf{w} = \int_{v_h} \mathbf{j} \cdot \mathbf{w} dv_h = \int_{v_h} \mathbf{j} \cdot \nabla(\mathbf{w} \cdot (\mathbf{x} - \tilde{\mathbf{n}}_{v_h})) dv_h \tag{65}$$

$$= \int_{\partial v_h} (\mathbf{j} \cdot \mathbf{n}_{\partial v_h})(\mathbf{w} \cdot (\mathbf{x} - \tilde{\mathbf{n}}_{v_h})) dS \tag{66}$$

$$= \sum_{f \in \partial v_h} (\mathbf{j} \cdot \mathbf{f})((\mathbf{b}_f - \tilde{\mathbf{n}}_{v_h}) \cdot \mathbf{w}), \tag{67}$$

where  $\mathbf{f}$  is the face vector of face  $f$ . By using the definition of  $\tilde{\mathbf{e}}_f^{v_h}$  and  $I_f = \mathbf{j} \cdot \mathbf{f}$  which holds since  $\mathbf{j}$  is uniform in  $v_h$ , it follows that

$$|v_h| \mathbf{j} \cdot \mathbf{w} = \sum_{f \in \partial v_h} (\mathbf{j} \cdot \mathbf{f})(\tilde{\mathbf{e}}_f^{v_h} \cdot \mathbf{w}). \tag{68}$$

Since  $\mathbf{w}$  is arbitrary, we obtain the claimed equality.  $\square$

We define  $\mathbf{w}_{f_j}(\mathbf{r})$  as the uniform basis function whose support is the union of the unique two volumes  $v_h$  and  $v_k$  that are adjacent to  $f_j$  face. In each of these volumes,  $\mathbf{w}_{f_j}(\mathbf{r})$  is a constant vector given by

$$\mathbf{w}_{f_j}^{v_i}(\mathbf{r}) = \frac{1}{|v_i|} \tilde{\mathbf{e}}_{f_j}^{v_i}, \mathbf{r} \in v_i, i \in \{h, k\}. \tag{69}$$

We can restate Lemma 1 by saying that the functions  $\mathbf{w}_{f_j}^{v_i}$  form a basis for the vector subspace of the constant vector fields defined in  $v_i$ .

### 5.2. Construction of a symmetric and consistent constitutive matrices

An efficient recipe to construct consistent and symmetric mass matrices exploits the uniform basis function introduced in (64), which are able to represent a uniform vector field defined in a given volume.

#### 5.2.1. Resistance mass matrix

The  $(i, j)$  entry of the local resistance matrix  $\mathbb{R}^{v_h}$ , built for  $v_h$  whose resistivity tensor is  $\mathbb{K}_\rho$ , is constructed as

$$R_{ij}^{v_h} = \int_{v_h} \mathbf{w}_{f_i}^{v_h}(\mathbf{r}) \cdot \mathbb{K}_\rho \mathbf{w}_{f_j}^{v_h}(\mathbf{r}) dv_h. \tag{70}$$

Being the integration exact since the basis functions are uniform inside  $v_h$ , it follows that

$$R_{ij}^{v_h} = |v_h| \mathbf{w}_{f_i}^{v_h} \cdot \mathbb{K}_\rho \mathbf{w}_{f_j}^{v_h}. \tag{71}$$

The global  $\mathbb{R}$  matrix is then constructed as

$$\mathbb{R} = \sum_{h=1}^V \mathbb{O}^{v_h T} \mathbb{R}^{v_h} \mathbb{O}^{v_h}. \tag{72}$$

#### 5.2.2. Magnetic mass matrix

The  $(i, j)$  entry of the local magnetic mass matrix  $\mathbb{M}^{v_h v_k}$  between two considered volumes  $v_h$  and  $v_k$  is

$$M_{ij}^{v_h v_k} = \frac{\mu_0}{4\pi} \int_{v_h} \int_{v_k} \frac{\mathbf{w}_{f_i}^{v_h}(\mathbf{r}) \cdot \mathbf{w}_{f_j}^{v_k}(\mathbf{r}')}{|\mathbf{r} - \mathbf{r}'|} dv_h dv_k. \tag{73}$$

Let  $t^{v_h v_k}$  be the positive number defined as follows

$$t^{v_h v_k} = \frac{\mu_0}{4\pi} \int_{v_h} \int_{v_k} \frac{1}{|\mathbf{r} - \mathbf{r}'|} dv_h dv_k, \tag{74}$$

then (73) becomes

$$M_{ij}^{v_h v_k} = t^{v_h v_k} \mathbf{w}_{f_i}^{v_h} \cdot \mathbf{w}_{f_j}^{v_k}. \tag{75}$$

And, in conclusion, the global  $\mathbb{M}$  matrix construction follows as

$$\mathbb{M} = \sum_{h=1}^V \sum_{k=1}^V \mathbb{O}^{v_h T} \mathbb{M}^{v_h v_k} \mathbb{O}^{v_k}. \tag{76}$$

### 5.3. Construction of symmetric positive definite and consistent constitutive matrices

The construction of symmetric *positive definite* consistent mass matrices is inspired by a well established design strategy which decomposes a local mass matrix as the sum of a *consistent* and a *stabilization* part [56,57]. Each part plays a specific role: the consistent part enforces the polynomial consistency property while the stabilization part ensures positive-definiteness, preserving the consistency already achieved.

In this section, we add to the local mass matrix  $\mathbb{R}^{v_h}$  a stabilization matrix which is symmetric and positive semidefinite and we look for a suitable *new stabilization matrix*, which is shown to be symmetric and positive semidefinite too, to be added to the dense  $\mathbb{M}^{v_h v_k}$ .

**Definition 5.1 (Stabilization Matrix).** Let  $F_{v_h}$  be the number of faces of  $v_h$ . Let  $\mathbb{F}^{v_h}$  be the  $F_{v_h} \times 3$  matrix whose rows collect face vectors associated with the volume  $v_h$ . A matrix  $\mathbb{S}^{v_h}$  of size  $F_{v_h} \times F_{v_h}$  is called a *stabilization matrix for the volume  $v_h$*  if it is symmetric, positive semidefinite matrix and such that  $\ker(\mathbb{S}^{v_h}) = \text{im}(\mathbb{F}^{v_h})$ .

We provide two canonical examples of stabilization matrices that can be used on every polyhedral volume  $v_h$ . As a first example, let  $\alpha = (\alpha_1, \dots, \alpha_{F_{v_h}-3}) \in (\mathbb{R}^+)^{F_{v_h}-3}$  be any  $(F_{v_h} - 3)$ -uple of positive real numbers. Let  $(\mathbf{k}_1, \dots, \mathbf{k}_{F_{v_h}-3})$  be an orthonormal basis of the *orthogonal complement* of  $\text{im}(\mathbb{F}^{v_h})$ . We define a stabilization matrix  $\mathbb{S}^{v_h}$  by setting

$$\mathbb{S}^{v_h} = \sum_{i=1}^{F_{v_h}-3} \alpha_i \mathbf{k}_i (\mathbf{k}_i)^T. \tag{77}$$

While this approach is very general, it requires the computation of the kernel of a matrix. If  $v_h$  is a tetrahedron, then the recipe proposed in [58] can be applied, which is a particular case of the above construction. As a more geometric approach, we introduce the following stabilization matrix, which is a reinterpretation of the vector basis functions introduced in [43]. We denote by  $\tilde{\mathbb{E}}^{v_h}$  the matrix whose columns collect edge vectors associated with the restriction of dual edges to  $v_h$ . Let

$$\mathbb{A}^{v_h} = \mathbb{I}_{F_{v_h}} - \frac{1}{|v_h|} \mathbb{F}^{v_h} \tilde{\mathbb{E}}^{v_h}, \tag{78}$$

where  $\mathbb{I}_{F_{v_h}}$  is identity matrix of order  $F_{v_h}$ . By applying Lemma 1 we have that  $\text{im}(\mathbb{F}^{v_h}) \subset \ker(\mathbb{A}^{v_h})$ . In particular,  $\text{rank}(\mathbb{A}^{v_h}) = F_{v_h} - 3$  and thus, we define a valid stabilization matrix by setting

$$\mathbb{S}^{v_h} = \mathbb{A}^{v_h T} \mathbb{A}^{v_h}. \tag{79}$$

#### 5.3.1. Positive definite resistance mass matrix

Let  $\mathbb{R}_S^{v_h}$  be the matrix defined as follows

$$\mathbb{R}_S^{v_h} = \mathbb{R}^{v_h} + \mathbb{S}^{v_h}. \tag{80}$$

The corresponding global matrix  $\mathbb{R}_S$  is constructed as follows

$$\mathbb{R}_S = \sum_{h=1}^V \mathbb{O}^{v_h T} \mathbb{R}_S^{v_h} \mathbb{O}^{v_h}. \tag{81}$$

**Theorem 1.** Matrix  $\mathbb{R}_S$  is symmetric and positive-definite.

**Proof.** It is sufficient to prove that  $\mathbb{R}_S^{v_h}$  is positive definite. Let  $\mathbf{z} \in \mathbb{R}^{F_{v_h}}$  such that  $\mathbf{z}^T \mathbb{R}_S^{v_h} \mathbf{z} = 0$ . In order to prove that  $\mathbb{R}_S^{v_h}$  is positive definite, we have to show that  $\mathbf{z} = \mathbf{0}$ . The condition  $\mathbf{z}^T \mathbb{R}_S^{v_h} \mathbf{z} = 0$  is equivalent to require

that

$$\mathbf{z}^T \mathbb{R}^{v_h} \mathbf{z} = 0, \tag{82}$$

$$\mathbf{z}^T \mathbb{S}^{v_h} \mathbf{z} = 0. \tag{83}$$

Based on the properties of the stabilization matrix, it follows that  $\mathbf{z} \in \text{im}(\mathbb{F}^{v_h})$ , thus  $\mathbf{z} = \mathbb{F}^{v_h} \mathbf{y}$  for some  $\mathbf{y} \in \mathbb{R}^3$ . By substituting in (82), it follows that

$$(\mathbb{F}^{v_h} \mathbf{y})^T \mathbb{R}^{v_h} \mathbb{F}^{v_h} \mathbf{y} = 0, \tag{84}$$

from which, using Lemma 1 and the definition of  $\mathbb{R}^{v_h}$ , we conclude that  $\mathbf{y} = \mathbf{0}$  and  $\mathbf{z} = \mathbb{F}^{v_h} \mathbf{y} = \mathbf{0}$ .  $\square$

### 5.3.2. Positive definite magnetic mass matrix

Let  $\mathbb{M}_S^{v_h v_k}$  be the matrix defined as follows

$$\mathbb{M}_S^{v_h v_k} = \begin{cases} \mathbb{M}^{v_h v_k} + \mathbb{S}^{v_k} & \text{if } h = k \\ \mathbb{M}^{v_h v_k} & \text{if } h \neq k \end{cases}. \tag{85}$$

The corresponding global matrix  $\mathbb{M}_S$  is constructed as follows

$$\mathbb{M}_S = \sum_{h=1}^V \sum_{k=1}^V \mathbb{O}^{v_h T} \mathbb{M}_S^{v_h v_k} \mathbb{O}^{v_k}. \tag{86}$$

**Theorem 2.** Matrix  $\mathbb{M}_S$  is symmetric and positive-definite.

**Proof.** Let  $\mathbf{z} \in \mathbb{R}^F$  such that  $\mathbf{z}^T \mathbb{M}_S \mathbf{z} = 0$ . In order to prove that  $\mathbb{M}_S$  is positive definite, we have to show that  $\mathbf{z} = \mathbf{0}$ . By using (86) we have

$$\begin{aligned} 0 &= \mathbf{z}^T \mathbb{M}_S \mathbf{z} \\ &= \sum_{h=1}^V \sum_{k=1}^V \mathbf{z}^T \mathbb{O}^{v_h T} \mathbb{M}_S^{v_h v_k} \mathbb{O}^{v_k} \mathbf{z} \\ &= \sum_{h=1}^V \mathbf{z}^T \mathbb{O}^{v_h T} \mathbb{M}_S^{v_h v_h} \mathbb{O}^{v_h} \mathbf{z} + \sum_{h=1}^V \sum_{k=1, k \neq h}^V \mathbf{z}^T \mathbb{O}^{v_h T} \mathbb{M}_S^{v_h v_k} \mathbb{O}^{v_k} \mathbf{z}. \end{aligned} \tag{87}$$

(87) is equivalent to require that

$$\sum_{h=1}^V \mathbf{z}^T \mathbb{O}^{v_h T} (\mathbb{M}^{v_h v_h} + \mathbb{S}^{v_h}) \mathbb{O}^{v_h} \mathbf{z} = 0, \tag{88}$$

$$\sum_{h=1}^V \sum_{k=1, k \neq h}^V \mathbf{z}^T \mathbb{O}^{v_h T} \mathbb{M}^{v_h v_k} \mathbb{O}^{v_k} \mathbf{z} = 0, \tag{89}$$

where we have used (85). By repeating the same argument used in the proof of Theorem 1, it follows that each matrix  $\mathbb{M}^{v_h v_h} + \mathbb{S}^{v_h}$  is positive definite. Thus, from (88) it follows that  $\mathbf{z} = \mathbf{0}$ . As a consequence, (89) is also satisfied.  $\square$

## 5.4. Relations of the novel basis functions to the ones proposed in literature

### 5.4.1. Equivalence of RT, RWG, VU basis functions on tetrahedral meshes

This section remarks that when constructing  $\mathbb{C}^T (\mathbb{R}_S + i\omega \mathbb{M}_S) \mathbb{C}$  in tetrahedral meshes the stabilization part is not needed. In other words

$$\mathbb{C}^T (\mathbb{R}_S + i\omega \mathbb{M}_S) \mathbb{C} = \mathbb{C}^T (\mathbb{R} + i\omega \mathbb{M}) \mathbb{C}. \tag{90}$$

This fact has two consequences. First, the construction of the resistance and inductance matrices may be performed by using just the part encompassing the uniform fields inside the elements, since the construction of

the stabilization matrix can be avoided. Second, since the uniform field reconstructed from solenoidal currents on mesh faces is unique, it turns out that

$$\mathbb{C}^T (\mathbb{R} + i\omega\mathbb{M}) \mathbb{C} = \mathbb{C}^T (\mathbb{R}_{RWG} + i\omega\mathbb{M}_{RWG}) \mathbb{C}. \tag{91}$$

Yet another consequence is that the RT and RWG mass matrices can be interpreted as the one obtained with VU basis functions with a different choice for the stabilization part.

All of this implies that the accuracy of the novel method based on VU basis functions produces *exactly* the same matrices and the *same solution* of the one from standard Raviart–Thomas or RWG basis functions. Section 6 shows why the VU framework is to be preferred even in case of tetrahedral meshes.

### 5.5. State-of-the-art for polyhedra: Piecewise uniform (PWU) basis functions

For meshes composed by general polyhedra, the only technique that we are aware to produce a consistent, symmetric and positive definite matrix is introduced in [51]. It is based on the piecewise uniform (PWU) basis functions introduced in [43]. For hexahedra, prisms and pyramids one may use RT basis function that, however, produce inconsistent mass matrices.

## 6. From VU basis functions to inductance matrix factorization

EFIE formulations for solving eddy current problems, as discussed in this paper, are mainly afflicted by two shortcomings. First, the construction of the entries of  $\mathbb{M}$  matrix is slow due to the presence of the double integral that, in addition, for its self terms becomes singular; as a second aspect, the inductance matrix is fully populated and thus extremely expensive to be assembled and stored. Indeed, in this section, we illustrate how these two issues can be faced for arbitrary polyhedral meshes (wherein hexahedra, tetrahedra, prisms and pyramids are naturally included) thanks to the application of the novel VU basis functions.

### 6.1. Speeding up $\mathbb{M}$ assembly with VU basis function

Let us consider a pair of volumes  $v_h, v_k$  of a mesh  $\mathcal{K}$ . The  $(i, j)$  entry of the local magnetic mass matrix  $\mathbb{M}^{v_h v_k}$  is generally defined, as in (19), as

$$M_{ij}^{v_h v_k} = \frac{\mu_0}{4\pi} \int_{v_h} \int_{v_k} \frac{\mathbf{w}_{f_i}^{v_h}(\mathbf{r}) \cdot \mathbf{w}_{f_j}^{v_k}(\mathbf{r}')}{|\mathbf{r} - \mathbf{r}'|} dv_h dv_k. \tag{92}$$

If VU basis functions are employed in (92), then the computational cost for  $\mathbb{M}^{v_h v_k}$  assembly is reduced, even when  $\mathcal{K}$  is a tetrahedral mesh. Indeed, if standard RWG or RT basis functions are employed, one has to directly use (92). Instead, as reported in Section 5, when VU basis functions are considered, (92) becomes

$$M_{ij}^{v_h v_k} = t^{v_h v_k} \mathbf{w}_{f_i}^{v_h} \cdot \mathbf{w}_{f_j}^{v_k}, \tag{93}$$

wherein  $t^{v_h v_k}$  is

$$t^{v_h v_k} = \frac{\mu_0}{4\pi} \int_{v_h} \int_{v_k} \frac{1}{|\mathbf{r} - \mathbf{r}'|} dv_h dv_k, \tag{94}$$

If we now suppose  $v_h, v_k$  to be distinct volumes with  $F_{v_h}, F_{v_k}$  faces each, under the hypothesis that the floating point operations cost is ruled by the computation of  $1/|\mathbf{r} - \mathbf{r}'|^4$  it turns out that the obtained speed up when using (93) instead of (92) is around  $F_{v_h} \cdot F_{v_k}$ . In fact, with our approach one has to compute just one double numerical integral (94) whereas in the standard case (92) one has to compute  $F_{v_h} \cdot F_{v_k}$  numerical integrals.

<sup>4</sup> CPU cycles to perform division and square root dominate the dot products between the basis functions.

## 6.2. Singularity extraction with VU basis functions

The evaluation of the double integral (92) is singular whenever  $v_h = v_k$ , i.e. for all the diagonal terms of  $\mathbb{M}$  [21].

From a survey of literature on this topic, it is soon clear that the presence of affine basis functions in (92) leads to complex recipes to get rid of the singularity because each proposed technique is necessarily influenced by the integration domain shape (triangular, tetrahedral, prismatic, polyhedral) and by the basis functions definition; see, for instance, [21,59] for 3D integration domains or [60,61] for 2D. Hence, the possibility of dealing with volume uniform basis functions has a great potential in this respect since it allows to drastically simplify and speed up the computation. Yet, in case of a simplicial mesh, the germ of this idea is presented in [21], but no volume uniform basis functions are proposed. On the contrary, the idea seems to be entirely new when working with hexahedra, pyramids and polyhedral volumes in general.

We use the well established approach called *singularity extraction* (sometimes also referred to as *singularity subtraction*) that consists of extracting a singular term from the double integral and integrate it in closed form to then treat the obtained expression numerically by mean of quadrature rules [59,61]. The singularity extraction has been already applied in literature, but not with volume uniform basis functions. In fact, when the new VU basis functions are used, the singularity extraction can be applied to Eq. (93), in which the singular double integral  $t^{v_h v_k}$  can be computed separately from the calculation of the involved basis functions values. This yields a speed up of at least  $F_{v_h} \cdot F_{v_k}$ , where  $F_{v_h}, F_{v_k}$  are the number of faces of elements  $v_h, v_k$ , because only one numerical integral has to be computed (namely  $t^{v_h v_k}$ ) in place of  $F_{v_h} \cdot F_{v_k}$  numerical integrals in (92). The obtained gain is even more, because the integral (94) is simpler. In fact, since the  $w_f$  are no more part of the singular integral, several closed-form exact expressions as the ones in [62], can now be applied to analytically calculate the innermost integral thus eliminating the singularity.

Given that it has just been shown that our (93) has to be preferred with respect to (92), now we investigate the difference between the results obtained with singularity extraction and the common solution that uses a double numerical integration. To this aim, a standard tetrahedron  $T$  whose vertices are  $(0, 0, 0), (1, 0, 0), (0, 1, 0), (0, 0, 1)$  is considered on which the double integral

$$DD = \int_T \int_{T'} \frac{1}{|\mathbf{r} - \mathbf{r}'|} dv dv',$$

is computed in three different ways: with a double numeric integration, with the singularity extraction approach and, finally, with an analytic formula developed for this case only, by successively applying the Gauss Divergence Theorem [63,64] and by means of a symbolic calculus software. This last one will be considered as the reference value for the double integral.

In Fig. 7, we report the results of this computation with several integration orders: the top plot shows the actual values obtained, the bottom plot shows the percentage error computed as

$$\varepsilon\% = 100|DD - DD_{ref}|/|DD_{ref}|.$$

Indeed, as reported in literature, the singularity extraction approach yields accurate values also for low numerical integration orders, whereas the purely numeric integration results to be highly inaccurate.

To complete the picture, in Fig. 8 we propose the same computation wherein one of the two domains of the double integral changes its position with respect to a first fixed tetrahedron. In this case we just compare the values obtained by applying the singularity extraction with the ones obtained with a double numerical integration: the error is computed against the value obtained with the singularity extraction combined with the highest order of numerical integration (namely, *Sing. Extr.*,  $\mathcal{O}(x^{16})$ ) given that the previous plot showed the accuracy of this approach. The plot shows that when the two domains superpose, the double numerical integration yields inaccurate and oscillating results, whereas without a superposition of the two tetrahedra a good accuracy is obtained also with double numeric integration since for disjoint integration domains there is no singularity.

## 6.3. Factorization of the inductance matrix: MAGICA

We now recall the fact that, being  $\mathbb{M}$  or  $\mathbb{K}$  dense matrices, commonly advanced compression techniques must be taken into consideration whenever eddy currents have to be computed on large conducting domains that otherwise

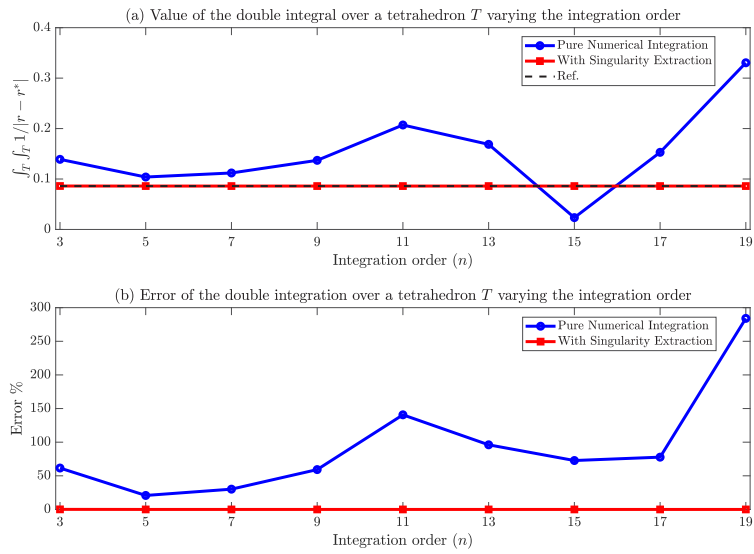


Fig. 7. Double integral calculation over a tetrahedron by varying integration order  $n$ . For the double numerical integration, at each point of the graph, a pair of  $n$  integration orders is intended to be applied.

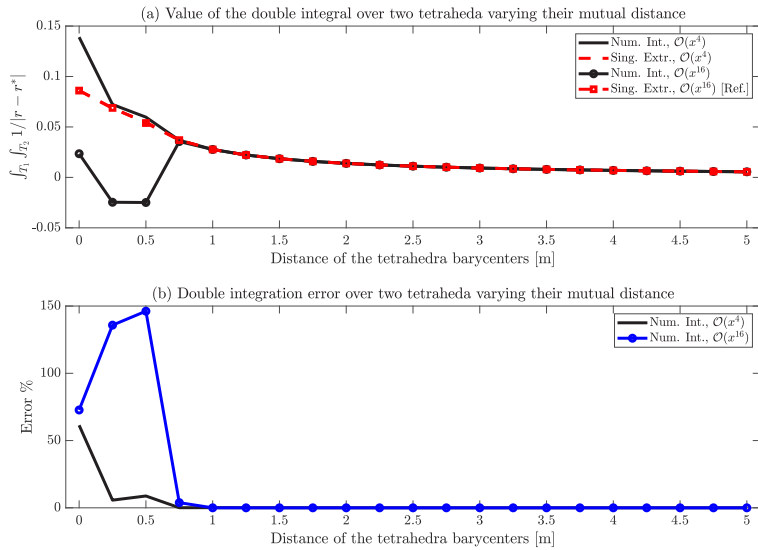


Fig. 8. Double integral calculation over a pair of tetrahedra whose mutual distance is successively increased. As a reference value to compute the error for this test, the “Sing. Extr.,  $O(x^{16})$ ” case is used since in the previous plot this approach was shown to be accurate.

would be not affordable by means of EFIE. This happens both because of the too large memory requirements for the matrix storage and because of the prohibitive computation time for the matrix assembly, see for example [24,27].

Usually one computes and stores the dense matrix  $\mathbb{M}$  whose dimension is  $F \times F$  to then assemble the complex system of Eq. (48) by means of the matrix–matrix product  $\mathbb{K}_M := \mathbb{C}^T \mathbb{M} \mathbb{C}$  finally obtaining a dense  $E \times E$ ; also,

as an alternative, the matrix–matrix product can be performed locally on each mesh volume and then matrix  $\mathbb{K}_M$  without computing the full  $\mathbb{M}$ . A third alternative for tetrahedral meshes is to assemble  $\mathbb{K}_M$  directly by using the curl of the Nédélec basis functions. We remark that, in all the three case, the number of elements in the system matrix scales quadratically with the number of the mesh edges  $E$ .

The seed of the idea here exposed stems from the fact that it might be much more convenient to compute and store a dense matrix  $\mathbb{N}$  of dimension  $V \times V$  containing all the results of the computation of the double integral  $t^{v_h v_k}$  for each couple  $v_h$  and  $v_k$  of the mesh and then reconstruct  $\mathbb{K}_M$  via a factorized expression involving sparse matrices whose memory occupation scales linearly with the number of unknowns of the problem. Since in a mesh  $\mathcal{K}$  the number of volumes  $V$  is typically lower than the number of edges  $E$  (or even faces), a memory saving is obtained.<sup>5</sup> In addition, it is here remarked that this reformulation is obtained by algebraic manipulation only, without any approximation or loss of accuracy.

Once the interaction matrix  $\mathbb{N}$  is computed and defined as

$$N_{hk} = \frac{t^{v_h v_k}}{|v_h||v_k|} \quad \forall h, k = 1, \dots, V, \tag{95}$$

it is then worth solving the system iteratively, in a matrix-free fashion, in order to just calculate matrix–vector products and never assemble the whole  $\mathbb{K}_M$  as it should be done in case of system solutions by means of direct linear solvers.

If, for the sake of simplicity, we for now consider the case of a tetrahedral mesh only, from (49), (75) and (85), an equivalent expression for  $\mathbb{K}_M$  based on the here introduced *Matrix fActorization for Geometrical Integral mAttrices* (MAGICA) can be obtained as

$$\mathbb{K}_M = \mathbb{C}^T \mathbb{O}_{F_B}^T \left( \tilde{\mathbb{E}}_x^T \mathbb{N} \tilde{\mathbb{E}}_x + \tilde{\mathbb{E}}_y^T \mathbb{N} \tilde{\mathbb{E}}_y + \tilde{\mathbb{E}}_z^T \mathbb{N} \tilde{\mathbb{E}}_z \right) \mathbb{O}_{F_B} \mathbb{C}. \tag{96}$$

In this last expression:

- $\mathbb{O}_{F_B}$  is a *sparse* matrix of dimension  $F_B \times F$ .  $F_B$  is the total number of *blossomed faces* that are obtained by considering pairs  $(f_j, v_h)$  for  $j = 1, \dots, F$ ,  $h = 1, \dots, V$ , i.e., renumbering independently the faces of each volume of  $\mathcal{K}$ ; this means that all the faces shared between two volumes, i.e. not belonging to the conductor boundary  $\mathcal{K}$ , are repeated.<sup>6</sup>  $\mathbb{O}_{F_B}$  maps  $F$  faces of the mesh to blossomed  $F_B$  faces and each row, corresponding to a pair  $(f_j, v_h)$ , has only one non-zero entry that is equal to one.
- $\tilde{\mathbb{E}}_x$ ,  $\tilde{\mathbb{E}}_y$  and  $\tilde{\mathbb{E}}_z$  are *sparse* matrices of dimensions  $V \times F_B$ . Each column of  $\tilde{\mathbb{E}}_x$ ,  $\tilde{\mathbb{E}}_y$  and  $\tilde{\mathbb{E}}_z$ , corresponding to a pair  $(f_j, v_h)$ , contains just one non-zero entry which is equal to  $\mathbf{x} \cdot \tilde{\mathbf{e}}_{f_j}^{v_h}$ ,  $\mathbf{y} \cdot \tilde{\mathbf{e}}_{f_j}^{v_h}$  and  $\mathbf{z} \cdot \tilde{\mathbf{e}}_{f_j}^{v_h}$ , respectively, where  $\tilde{\mathbf{e}}_{f_j}^{v_h}$  is the edge vector associated with the restriction of dual edge  $\tilde{\mathbf{e}}_{f_j}^{v_h}$  of face  $f_j$  to  $v_h$  and  $\hat{\mathbf{x}} = (1, 0, 0)$ ,  $\hat{\mathbf{y}} = (0, 1, 0)$ ,  $\hat{\mathbf{z}} = (0, 0, 1)$ . By recalling the definition of  $\tilde{\mathbb{E}}^{v_h}$  given in Section 4 as the matrix storing in its columns edge vectors  $\tilde{\mathbf{e}}_j^{v_h}$ ,  $j = 1, \dots, F_{v_h}$  with  $F_{v_h}$  the number of faces of the polyhedron  $v_h$ , it follows that  $\hat{\mathbf{x}} \tilde{\mathbb{E}}^{v_h}$ ,  $\hat{\mathbf{y}} \tilde{\mathbb{E}}^{v_h}$  and  $\hat{\mathbf{z}} \tilde{\mathbb{E}}^{v_h}$  are the rows blocks of the desired global  $\tilde{\mathbb{E}}_x$ ,  $\tilde{\mathbb{E}}_y$  and  $\tilde{\mathbb{E}}_z$  as determined in the following for  $\tilde{\mathbb{E}}_x$ :

$$\tilde{\mathbb{E}}_x = \begin{pmatrix} \hat{\mathbf{x}} \tilde{\mathbb{E}}^{v_1} & 0 & 0 & \dots & \dots & \dots & \dots & 0 \\ \vdots & \hat{\mathbf{x}} \tilde{\mathbb{E}}^{v_2} & & & & & & \\ \vdots & & \hat{\mathbf{x}} \tilde{\mathbb{E}}^{v_3} & & & & & \\ \vdots & & & \ddots & & & & \\ \vdots & & & & \ddots & & & \\ \vdots & & & & & \ddots & & \\ \vdots & & & & & & \ddots & \\ 0 & & & & & & & \hat{\mathbf{x}} \tilde{\mathbb{E}}^{v_V} \end{pmatrix}.$$

<sup>5</sup> For instance, for a simplicial grid the number of edges is, on average, 30% greater than the volumes, hence obtaining  $E/V \approx 1.3$ ; for an hexahedral mesh this ratio increases up to  $E/V \approx 4-5$ . This traduces, for hexahedra, into a memory occupation reduction up to 25 times when storing the real dense  $\mathbb{N}$  in place of  $\mathbb{K}_M$ .

<sup>6</sup> As a consequence, in a simplicial mesh  $F_B = 4 V$ .

When the mesh is constituted by tetrahedra only, the stabilization matrix is not necessary. Thus, the expression in (96) is complete and the only hurdle left is the construction of  $\tilde{\mathbb{E}}_x$ ,  $\tilde{\mathbb{E}}_y$  and  $\tilde{\mathbb{E}}_z$  matrices.

Differently, for general polyhedra, the factorization in (96) is not complete and also the stabilization part has to be taken into account in order to be compliant with the definition of  $\mathbb{M}_S$  of (85). In this case is necessary to add new terms to (96) expressing the stabilization matrix  $\mathbb{S}^{v_h}$  of (85). The most efficient way to that goal is the direct assembly of the global stabilization matrix  $\mathbb{S}$  as

$$\mathbb{S} = \sum_{h=1}^V \mathbb{O}^{v_h T} \mathbb{S}^{v_h} \mathbb{O}^{v_h}. \tag{97}$$

Indeed, thanks to the definition in (85) in which the *local* stabilization matrix  $\mathbb{S}^{v_h}$  has to be summed to  $\mathbb{M}^{v_h v_k}$  only in the case  $v_h = v_k$ , Eq. (97) produces a sparse matrix with exactly the same sparsity of  $\mathbb{R}_S$ , as detailed in (81). Hence, it affects neither the assembly time nor the memory consumption for its storage since it scales linearly with the mesh dimension. In addition, it can be efficiently assembled simultaneously to  $\mathbb{R}_S$ , since the  $\mathbb{S}^{v_h}$  matrix has to be added both to  $\mathbb{R}^{v_h}$  and to  $\mathbb{M}^{v_h v_h}$ , hence it can be constructed only once per considered volume  $v_h$ .

As a matter of fact, in case of polyhedra, Eq. (96) becomes

$$\mathbb{K}_M = \mathbb{C}^T \mathbb{O}_{F_B}^T \left( \tilde{\mathbb{E}}_x^T \mathbb{N} \tilde{\mathbb{E}}_x + \tilde{\mathbb{E}}_y^T \mathbb{N} \tilde{\mathbb{E}}_y + \tilde{\mathbb{E}}_z^T \mathbb{N} \tilde{\mathbb{E}}_z \right) \mathbb{O}_{F_B} \mathbb{C} + \mathbb{C}^T \mathbb{S} \mathbb{C}. \tag{98}$$

It is here also noticed that *MAGICA* expression in (98) does not reflect the actual implementation. In fact, from a practical point of view, instead of storing  $\mathbb{C}$  and  $\mathbb{O}_{F_B}$  to then perform the matrix–matrix product with  $\tilde{\mathbb{E}}_x$ ,  $\tilde{\mathbb{E}}_y$  and  $\tilde{\mathbb{E}}_z$  it is wiser to directly assemble each of the three products  $\tilde{\mathbb{E}}_x \mathbb{O}_{F_B} \mathbb{C}$ ,  $\tilde{\mathbb{E}}_y \mathbb{O}_{F_B} \mathbb{C}$  and  $\tilde{\mathbb{E}}_z \mathbb{O}_{F_B} \mathbb{C}$  as sparse  $V \times E$  matrices. In addition, we also recall for the sake of precision, that Eq. (98) takes into account neither the boundary conditions nor the gauging: to this purpose, the same techniques described in Section 2 can be directly applied without any loss of generality.

## 7. A new family of compression techniques

In the previous section the *MAGICA* factorization of the dense inductance matrix  $\mathbb{K}_M$  of (48) was introduced. Indeed, it was shown that thanks to (96) for simplicial meshes and to (98) for polyhedral ones, a lossless compression of the memory occupation can be usually achieved. What is missing now is the system solution that can be achieved by means of two different iterative approaches: a lossless technique that directly applies (98) to (48) and an approximated scheme that can exploit either the Fast Multipole Method [17], ACA or any other fast summation algorithm in order to efficiently compute the off-diagonal terms of  $\mathbb{N}$ , with a consequent drastic reduction of the memory footprint and of the computation time. Let us carefully delineate them both.

### 7.1. LIME: A lossless integral matrix compression

The first possibility is represented by the application of the factorized expression of (98) into (48). In order to avoid the construction of a full, for instance,  $\tilde{\mathbb{E}}_x^T \mathbb{N} \tilde{\mathbb{E}}_x$  matrix, only on-the-fly matrix–vector products are allowed. Hence, matrix-free algorithms for the iterative solution of symmetric positive definite (SPD) systems, like GMRES [65], can be used. As far as the preconditioner is concerned, the diagonal part of  $\mathbb{K} = \mathbb{K}_R + i\omega \mathbb{K}_M$ , namely  $\text{diag}(\mathbb{K})$ , has been used.

In addition to this, also resorting to the solution of an *ungauged* system results to be very effective when working with Krylov’s subspace-based iterative solvers.

*VINCO solution with LIME.* The process described above yields the flow chart of Fig. 9 in which it is illustrated how to face the solution of an eddy current problem as expressed by EFIE in which *MAGICA* is applied for the compression and factorization of  $\mathbb{K}_M$ .

We here remark that in this section and thus in the proposed flow chart too, we did not specify whether the domain is simply connected or not; in fact, this distinction is not necessary since Eq. (98) can be plugged into (48) without loss of generality.

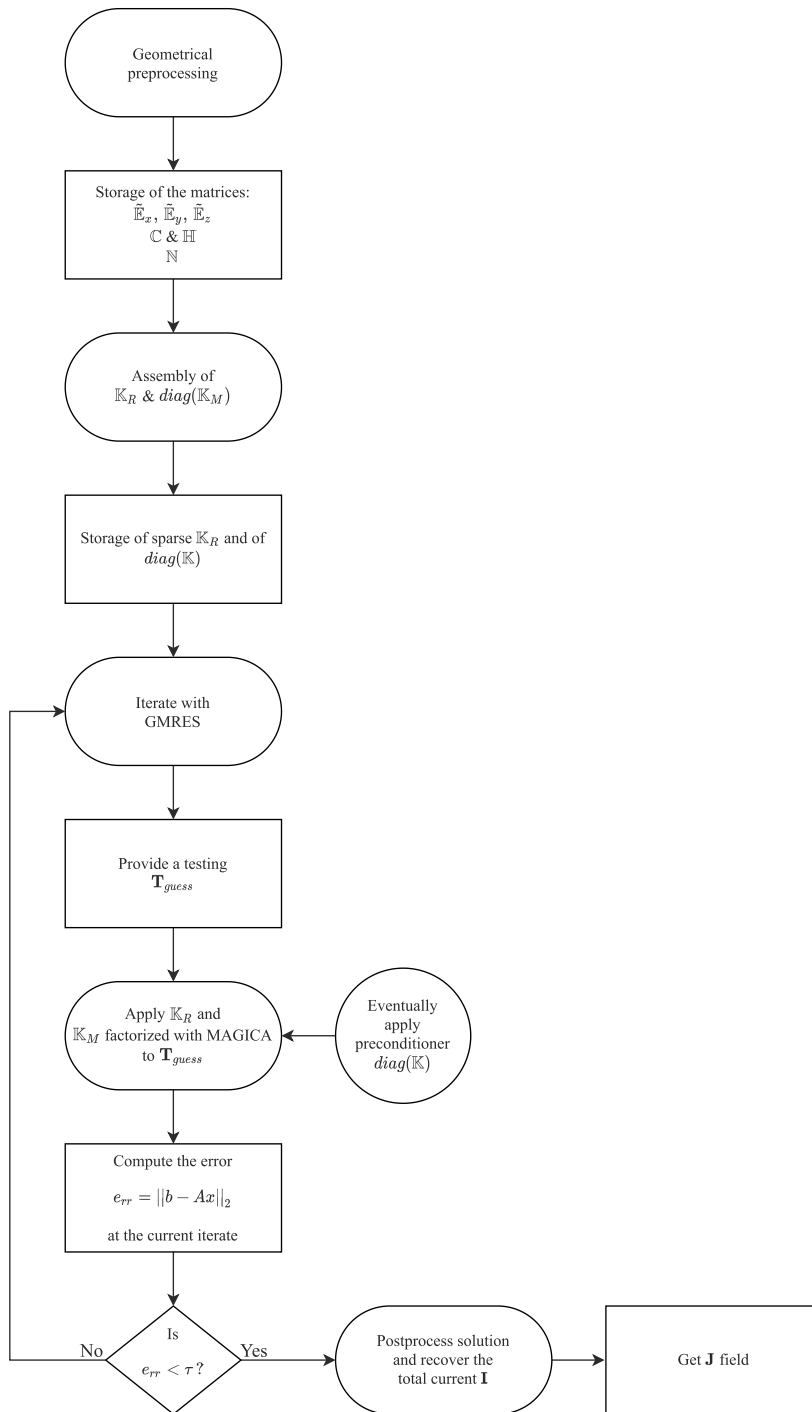


Fig. 9. Flow chart of the iterative system solution with LIME.

## 7.2. Approximated compressions of integral matrices

In order to further increase the size of the problems affordable with the EFIE formulation here exposed, it may be very useful to apply more advanced compression techniques than the lossless factorization based on the full computation of  $\mathbb{N}$  matrix exposed in the last section.

Literature mainly illustrates two possible approaches to be employed in case of EFIE: from the one hand there are *algebraic* methods based on hierarchical matrices algebra like the Adaptive Cross Approximation that are the most diffused, to the other hand also *analytical* approaches that relies on an analytic expansion of the  $1/r$ -kernel-based expressions, as it is done by the Fast Multipole Method, can be extremely interesting since these methods are able to rapidly and efficiently calculate the interactions that have to be computed when assembling the dense magnetic matrix  $\mathbb{M}$ . Yet, even if both of them may seem to be equally appealing and theoretically effective in reducing both the peak memory usage and the computational time during the system assembly, in truth, when applied to the formulation without any factorization as exposed until Section 3, both of them exhibit important limitations and downsides.

First, ACA-based approaches are not very efficient when applied to the system matrix  $\mathbb{K}$ . Indeed, the tricky aspect resides in the fact that rows and columns of  $\mathbb{K}$  are referred to the mesh edges whereas usually the assembly of  $\mathbb{M}$  has to be constructed sequentially by looping within the mesh volumes. When an ACA library is interfaced to  $\mathbb{K}$ , this traduces either into huge assembly inefficiencies. In both cases, the result is that, even if a memory usage reduction could be achieved, the same does not happen for the assembly time which is reduced to half at most, see for example [24] or [27].

Second, as extensively explained in [24], standard ACA-based approaches applied on  $\mathcal{K}$  show poor performances whenever the problem needs many cohomology generators (i.e., when the conducting domain presents several holes). This is caused by the non-local basis functions expressed in  $\mathbb{H}$  matrix that unavoidably have a very large support. As a consequence, most entries of  $\mathcal{K}$  have to be computed anyway. In [24] again, the problem is minimized by the retrieval of cohomology generators whose length is quasi-minimal, but also using a minimal cohomology basis the time required is huge.

Last but not least, we cannot forget that  $\mathbb{K}$  matrix is a complex operator. Since off-the-shelf ACA libraries offer facilities for the linear system solution, most contributions in literature apply ACA to the complex matrix  $\mathbb{K}$ . Thus, the memory allocation is almost *doubled* with respect to what would have been possible, considering that the real part of  $\mathbb{K}$ , i.e.  $\mathbb{K}_R$ , is instead very sparse.

Eventually, we must remark that FMM approaches are not free from criticism too. In this case the main limit is represented by the fact that the Fast Multipole Method works smoothly only in case of point charges. It follows that the standard definition of  $\mathbb{M}$  in which the  $\mathbf{w}_f$  face basis functions are involved is not well suited by itself for such an approach. In fact, the presence of linear  $\mathbf{w}_f$  in the double integral to be approximated with FMM yields, in the end, the necessity of resorting to complicated strategies in order to make FMM fit into the EFIE framework as it is done for instance in [66].

In conclusion, the proposal of a new form of (48) able to totally eliminate all the previously exposed drawbacks both for ACA-based and FMM-based approaches, represents without any doubt a ground-breaking step forward for EFIE formulation for eddy currents. Indeed, we claim that the factorization expressed by (96) and (98) perfectly reaches this goal. In the continuation we describe in detail how and why.

### 7.2.1. FAIME: A fast approximated integral matrix compression

In the authors' opinion, the most interesting and effective technique able both to reduce the memory requirements and to shrink the computation time too, which is the main bottleneck of EFIE formulations, is represented by the *Fast Approximated Integral Matrix comprEssion* approach (FAIME) in which FMM is applied to the computation of  $\mathbb{N}$ . More precisely, this new approach is based on the splitting of the dense matrix  $\mathbb{N}$  into

$$\mathbb{N} = \mathbb{N}^D + \mathbb{N}^{OD} \quad (99)$$

in which  $\mathbb{N}^D$  is a very sparse matrix representing the *near-field interactions* and  $\mathbb{N}^{OD} = \mathbb{N} - \mathbb{N}^D$  is the dense remaining part representing the *far-field interactions* on which FMM is applied.<sup>7</sup> A possible choice is to consider in

<sup>7</sup> We remark that this is different with respect to what done previously in the literature, where the matrix  $\mathbb{K}$  or  $\mathbb{K}_M$  is split. We split matrix  $\mathbb{N}$ .

$\mathbb{N}^D$  the diagonal term plus some of the off-diagonal terms of  $\mathbb{N}$ , specifically the ones relative to the neighbouring volumes.

In addition, when two volumes of the mesh  $v_h$  and  $v_k$  are not close from each other, the following approximation holds

$$t^{v_h v_k} = \frac{\mu_0}{4\pi} \int_{v_h} \int_{v_k} \frac{1}{|\mathbf{r} - \mathbf{r}'|} dv_h dv_k \approx \frac{\mu_0}{4\pi} \frac{|v_h||v_k|}{|\mathbf{b}_{v_h} - \mathbf{b}_{v_k}|}, \quad (100)$$

in which  $\mathbf{b}_{v_h}$  and  $\mathbf{b}_{v_k}$  are the coordinates of the barycenters of  $v_h$  and  $v_k$  volumes, respectively.

Once this approximation is introduced, then *any* off-the-shelf FMM library can be applied in order to rapidly and efficiently compute the effects of the off-diagonal terms relative to  $\mathbb{N}^{OD}$ . Moreover, any alternative fast-summation technique developed for N-body simulation, molecular dynamics or electrosatics, like Mesh particle method (M3P), fast Ewald summation, etc. can be easily employed thanks to the MAGICA factorization.

From the implementation point of view, FMM results to be the most effective tool in drastically reducing the part of  $\mathbb{N}$  to be stored that can be thus limited to the sparse  $\mathbb{N}^D$ . This traduces into the possibility of rearrange  $\mathbb{K}$  too by following the same splitting as of (99), thus obtaining

$$\mathbb{K} = \mathbb{K}^{NEAR} + i\omega \mathbb{K}_M^{FAR}, \quad (101)$$

in which

$$\mathbb{K}^{NEAR} = \mathbb{K}_R + i\omega \mathbb{C}^T \mathbb{O}_{F_B}^T \left( \tilde{\mathbb{E}}_x^T \mathbb{N}^D \tilde{\mathbb{E}}_x + \tilde{\mathbb{E}}_y^T \mathbb{N}^D \tilde{\mathbb{E}}_y + \tilde{\mathbb{E}}_z^T \mathbb{N}^D \tilde{\mathbb{E}}_z \right) \mathbb{O}_{F_B} \mathbb{C} + \mathbb{C}^T \mathbb{S} \mathbb{C} \quad (102)$$

and

$$\mathbb{K}^{FAR} = \mathbb{C}^T \mathbb{O}_{F_B}^T \left( \tilde{\mathbb{E}}_x^T \mathbb{N}^{OD} \tilde{\mathbb{E}}_x + \tilde{\mathbb{E}}_y^T \mathbb{N}^{OD} \tilde{\mathbb{E}}_y + \tilde{\mathbb{E}}_z^T \mathbb{N}^{OD} \tilde{\mathbb{E}}_z \right) \mathbb{O}_{F_B} \mathbb{C}. \quad (103)$$

It turns out that, by resorting to the proposed FAIME approach, we can represent the otherwise dense EFIE matrix  $\mathbb{K}$  just by only storing a set of sparse *real* matrices, i.e.  $\mathbb{K}_R = \mathbb{C}^T \mathbb{R}_S \mathbb{C}$ ,  $\mathbb{K}_S = \mathbb{C}^T \mathbb{S} \mathbb{C}$ ,  $\mathbb{O}_{F_B}$ ,  $\tilde{\mathbb{E}}_x$ ,  $\tilde{\mathbb{E}}_y$ ,  $\tilde{\mathbb{E}}_z$  and  $\mathbb{N}^D$ , because  $\mathbb{K}^{FAR}$  and thus  $\mathbb{N}^{OD}$  too, are never actually assembled but it is computed their application to a given DoFs array provided by GMRES (namely,  $\mathbf{T}_{guess}$  of Fig. 9) on the fly at each iterate by means of the FMM. In addition, it is worth recalling that the computation of  $\mathbb{N}^D$  is very efficient too, because it is highly parallelizable without any peculiar effort due to the fact that  $\mathbb{N}^D$  rows and columns directly refer to the volumes mesh and not to edges or faces as it happens for  $\mathbb{M}$  or  $\mathbb{K}_M$ , respectively.

We also mention that the use of FMM for the fast computation of  $\mathbb{N}^{OD} = \mathbb{N} - \mathbb{N}^D$  applied to a given DoFs array results to be a successful recipe because by doing this the FMM library is applied to a minimal grid of points when computing point-to-point interactions between the barycenters of the mesh volumes thus saving time and reducing memory occupation for the same reasons explained in Section 6.3.

### 7.2.2. Algebraic methods

When discussing about algebraic method, also ACA is suitable to be used in order to compress  $\mathbb{N}$ .<sup>8</sup> The strategy is exactly the same as that one described for FMM with the only difference that in this case the computation of the application of  $\mathbb{N}$  to  $\mathbf{T}$  is not performed on the fly as for the FMM but it has to be treated as a preprocessing step before iteratively solving the system. When ACA library is invoked, a compressed hierarchical expression of the whole  $\mathbb{N}$  is computed and stored in the calculator memory. Yet, even if it can be shown that the overall compression ratio between FMM and ACA is very similar, the same cannot be said for the peak memory usage, that is much higher when ACA is applied. Thus, using FMM extends the applicability of the solver, where ACA is inapplicable because it would use too much memory. By the way, also for this case, the application of ACA for the calculation of  $\mathbb{N}$  instead of  $\mathbb{K}$  automatically resolves, in a efficient and accurate way, all the troubles and limitations above exposed both in terms of implementation complications and in terms of theoretical shortcomings caused by cohomology generators and vector basis functions.

<sup>8</sup> Again, we remark that this is different with respect to what appears in literature, where ACA compression can be applied only on matrix  $\mathbb{K}$  or  $\mathbb{K}_M$ , and not on matrix  $\mathbb{N}$  as we propose.

## 8. Numerical results

In this last part, we propose a selection of numerical results aimed at giving proof to the claims of the previous sections and at assessing the correctness and accuracy of the implementation of the new VINCO code.

In order to obtain the preliminary results of Section 8.1, the code was first implemented in the MATLAB® framework. Then, the whole code was rewritten in FORTRAN language with the aid of OpenMP instructions when needed, especially for post processing purpose. Intel®MKL routines are exploited for specific tasks, like sparse matrix–vector products and sparse matrix factorizations that will be shown to be required when preconditioning in the low-frequency regime. As far as the FMM implementation is concerned, we make use of the parallel *FMM3D* library proposed by the Flatiron Institute [32].

Simulations are performed on a Windows server (hereafter, *the Windows Server*) in which an AMD Ryzen™ Threadripper PRO 3975WX (32 cores/64 threads @3.49 GHz) processor runs endowed with 256 GB of RAM. Yet, it is fundamental to highlight that most of the results can be also obtained on a standard Windows laptop (now on, *the Windows Laptop*) equipped with an Intel®Core™i7 processor (4 cores @2.9 GHz) with 16 GB of RAM without incurring in any memory saturation.

In the following, for the first set of results, we resort to the eddy currents computation in the frequency domain in a solid conductive sphere of radius  $R_0 = 50.0$  mm immersed in a uniform induction field  $B_z = 1.0$  mT vertically directed along the  $z$ -axis. The choice of this geometry as a test bench is driven by the fact that an analytical solution is provided in [67], thus allowing for thorough comparisons and analysis. Later on, once that the code validity is assessed, eddy currents phenomena are calculated in more general not simply connected geometries, more specifically, on the TEAM Workshop Problem 7 [68], on a conducting plate with seven holes and a coil realized on a printed circuit board.

### 8.1. Singularity extraction effect

In Fig. 10 it is shown how the behaviour represented in Fig. 7 reflects into the computed value of the ohmic losses  $P_{diss}$  in a solid sphere. For this test, a conducting sphere with resistivity  $\rho = 1.68 \cdot 10^{-8} \Omega \cdot \text{m}$  meshed with a coarse simplicial grid with a DoFs number  $N_{dofs} = 317$  is used. The frequency  $f$  of the vertical induction field applied is  $f = 25$  Hz.

The computation of  $P_{diss}$  that is dissipated due to the eddy current flowing in the discretized representation of the conductors  $\mathcal{K}$ , in this case and in all the subsequent sections wherein we make use of it, is calculated as

$$P_{diss} = \int_{\Omega_c} \rho \mathbf{j}^2 dv = \sum_{k=1}^V \rho_k |v_k| \mathbf{j}_{rms,k}^2, \quad (104)$$

with  $|v_k|$  the volume of the  $k$ th volume  $v_k$  of  $\mathcal{K}$  and  $\mathbf{j}_{rms,k}$  the RMS of the current density value associated to  $v_k$ .

The graph proves that, when the singularity is not properly treated and the double integral is performed with a double numerical integration, also the computed power value oscillates as it happens for the values of the double integral plotted in Fig. 7. Yet, it is also pointed out that singularity is not properly accounted for in most recent papers, see for example [24,50], where, in fact, this aspect is not plainly reported and discussed.

For the sake of precision, we remark that since for this test high order integration was needed for a rigorous comparison and a distinct  $\mathbb{K}_M$  matrix was built for each integration order, the employed mesh was chosen with a limited number of elements ( $N_{dofs} = 317$ ) in order to limit the assembly time. For this reason, the dissipated power value obtained both with the singularity extraction (blue line in Fig. 10) and with the double numerical integration are not close to the analytic reference ( $P_{diss}^{REF} = 28.44$  mW for this problem setting). Nevertheless, the different behaviour in terms of solution stability when varying the integration order of the two approaches is undeniable.

### 8.2. FAIME approach accuracy and convergence

As a successive step, the attention is now focused on the solution accuracy that can be achieved with the FAIME implementation. In more details, the solution of the solid sphere with differently grained meshes is faced first, both with tetrahedral and hexahedral elements; then, also TEAM 7 benchmark is proposed as a more complicate geometry example. As a third paramount aspect that is analysed in the following, the behaviour of the iterative solver convergence when the frequency varies is reported too.

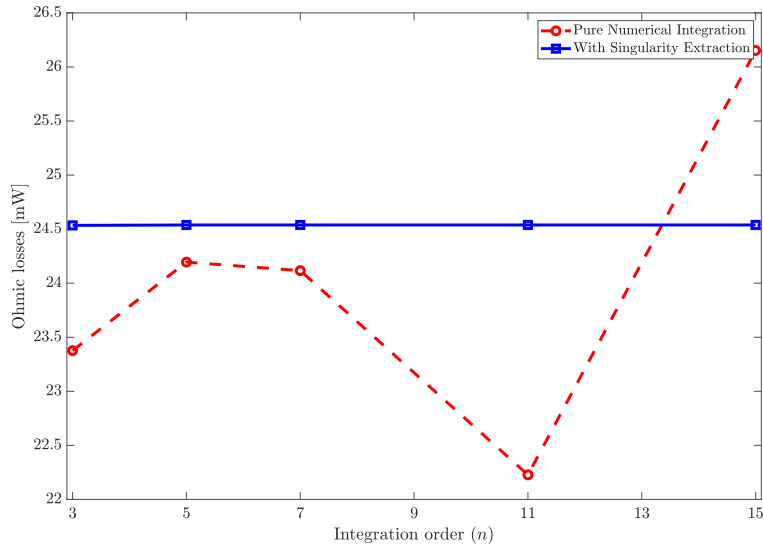


**Fig. 10.** Ohmic losses convergence varying the integration order ( $n$ ) on a deliberately coarse mesh constituted by 472 tetrahedra. For the double numerical integration, at each point of the graph, a pair of ( $n, n$ ) integration orders with different integration rules is intended to be applied.

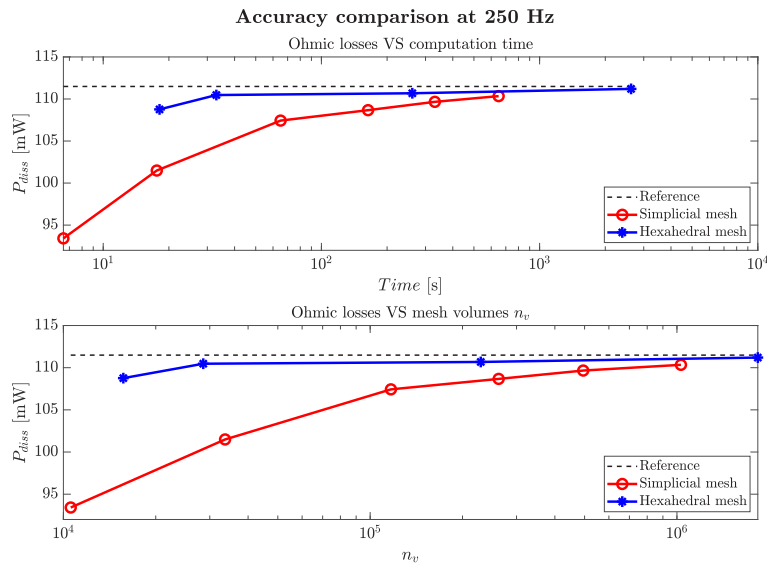


**Fig. 11.** Ohmic losses trend for simplicial and hexahedral meshes successively refined. Top:  $P_{diss}$  convergence versus the computation time. Bottom:  $P_{diss}$  convergence versus number of mesh elements  $V$ . For this chart  $P_{diss}^{REF} = 111.49$  mW.

### 8.2.1. Ohmic losses in a solid sphere

In Fig. 11 a comparison versus both the total computational time and the mesh volumes in the solid conducting sphere of radius  $R_0 = 50$  mm is proposed. For this test, the frequency is  $f = 250$  Hz, the resistivity  $\rho = 1.68 \cdot 10^{-8} \Omega \cdot m$  and the external induction field is uniform:  $B_z = 1.0$  mT. Convergence and accuracy are always very good.

In regard to the specifications of the grids employed for this benchmark, the number of volumes of the meshes varies from  $V = 10,566$  up to  $V = 1,030,656$  volumes for the tetrahedral mesh and from  $V = 15,680$  up to  $V = 1,835,008$  (hence, almost two millions elements) for the hexahedral one. Also, GMRES iterated 11 times for

**Table 1**  
Mesh data and calculation time in the Windows Server for the solid sphere benchmark.

Mesh type	$V$	$N_{dofs}$	Assembly [s]	Solve [s]	Tot. time [s]
Simplicial	10,566	9,517	4.35	2.0	6.57
	33,652	31,405	14.0	2.6	17.6
	116,863	111,677	54.5	8.9	65.0
	262,349	253,072	144.4	14.6	163.6
	494,865	481,383	249.5	63.0	331.0
Hexahedral	1,030,656	1,008,768	541.8	89.0	649.0
	15,680	30,773	14.0	3.2	18.12
	28,572	56,577	28.0	7.1	33.0
	229,376	455,681	211.0	48.0	261.0
	1,835,008	3,657,729	1,809.6	758.0	2,625.0

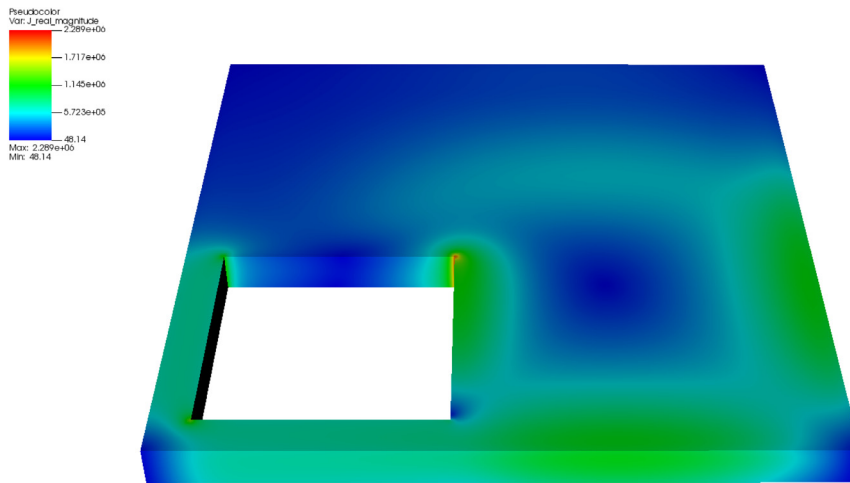


**Fig. 12.** Real( $j$ ) colour map at  $f = 50$  Hz in the TEAM 7 conducting plate. (For interpretation of the references to colour in this figure legend, the reader is referred to the web version of this article.)

every simplicial mesh and 14 times for the hexahedral grids. No variation of this parameter was observed during the trials when increasing  $V$ . Further details about these simulations are reported in Table 1.

Generally, from this comparison, it turns out that hexahedral meshes perform better than simplicial ones in terms of accuracy both when time and mesh volumes are considered and, in particular, when  $V$  is lower than 100,000. Yet, simplicial meshes have the advantage of a faster computation hence, especially when the number of volumes and DoFs grows, their performance becomes comparable to that one obtained with the hexahedral grids. Moreover, from a look at Table 1, it should be noticed that, as already stated, hexahedral meshes exhibit a DoFs number which is at least twice  $V$  whereas for simplicial ones this ratio is always equal to 1 or lower: another argument that makes simplicial grids preferable when  $V$  exceeds one million elements.

### 8.2.2. TEAM7 benchmark: Accuracy and frequency sweep

TEAM Workshop Problem 7 is faced. For the sake of concision the geometrical set up of the problem is not here reported given that it is carefully described in [68]. To solve the problem, a multi-block hexahedral mesh was created. The grid is constituted by 575,064 volumes for a corresponding  $N_{dofs} = 1,099,925$  to be solved and the source field computation is tackled by means of exact closed-form formula. In Fig. 12 the map of the real part of the current density in the conductor is showcased for the 50 Hz case whereas in Table 2 all the meaningful aspects of the simulation performance are listed.

Last but not least, in Figs. 13 and 14 the traditional induction field plots along A1–B1 and A2–B2 lines for the two test frequencies are proposed. Also in this case, an excellent correspondence between the simulated data and the TEAM 7 reference field is shown.

**Table 2**

Mesh data and calculation time in the Windows Server for the TEAM Workshop Problem 7.

Frequency [Hz]	$V$	$N_{dofs}$	Iterates	Assembly [s]	Solve [s]	Tot. time [s]
50.0	575,064	1,099,925	10	578.6	61.6	662.0
200.0	575,064	1,099,925	16	579.0	88.0	690.0

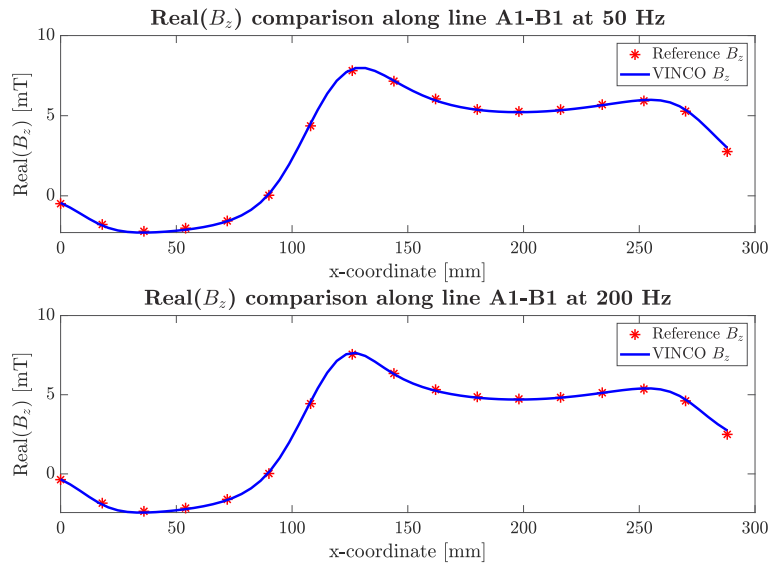


**Fig. 13.** Real part of the vertical induction field component along A1–B1 sample line.

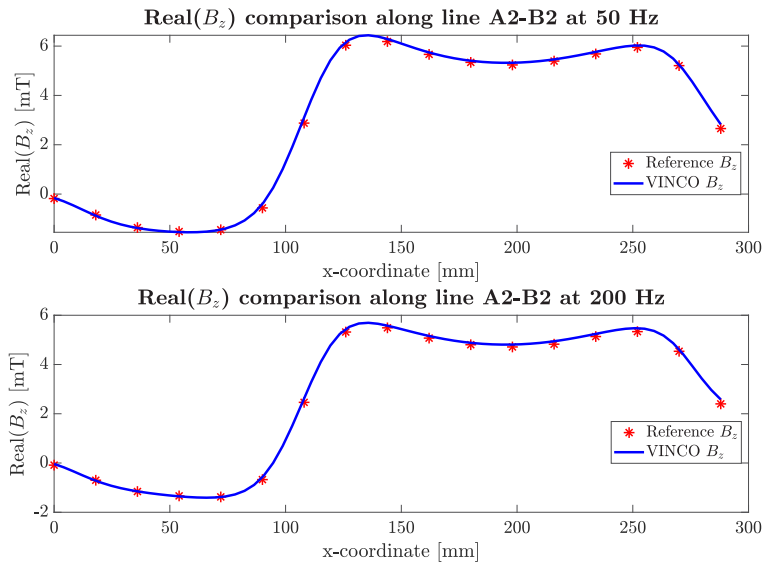


**Fig. 14.** Real part of the vertical induction field component along A2–B2 sample line.

Furthermore, the same problem is solved by discretizing the conductor with a mesh constituted by 132,000 hexahedra and 514,410 triangular prisms in order to assess the method effectiveness also in presence of a mixed

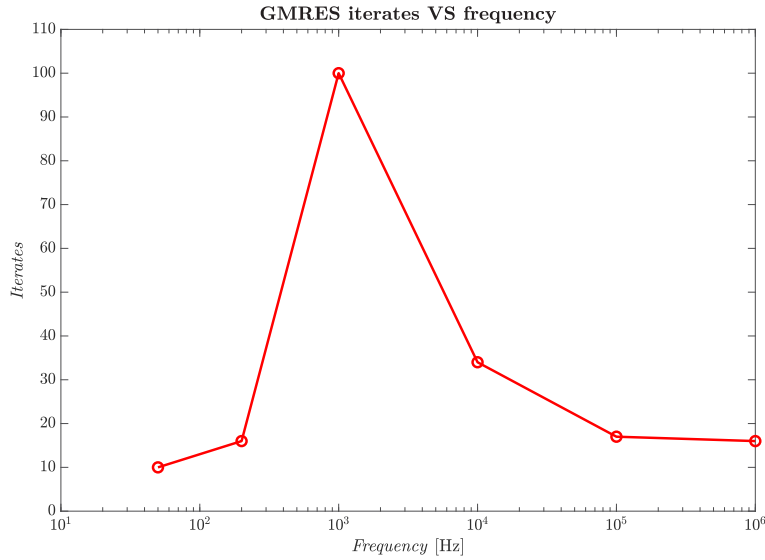


**Fig. 15.** Frequency variation and GMRES iterates values on TEAM 7 problem configuration.

mesh. Results reported in Fig. 16 are in perfect agreement with those ones previously obtained with a pure hexahedral grid.

Eventually, Fig. 15 is about a fundamental aspect when using iterative solvers like GMRES to obtain the solution of EFIE system: variation of the iterates number when changing the frequency. To that end, TEAM 7 problem is used as a common problem setting.

It is now worth mentioning that the chart is the result of two different strategies to precondition the system during its iterative solution: from the one hand, at low frequency i.e.  $f < 500.0$  Hz, a sparse preconditioner coincident to the real  $\mathbb{K}_R$  matrix is effectively applied to the *gauged* system of equations by means of its pre-factorized version obtained with PARDISO, to deeply accelerate the convergence of GMRES; to the other hand, when  $f$  exceeds that threshold another preconditioning technique is pursued that consists of solving an *ungauged* system whose rows are then rescaled thanks to a complex diagonal preconditioner  $\mathbb{K}_P = \text{diag}(\mathbb{K}_R + i\omega\mathbb{K}_M)$ .

This choice reflects into limiting the iterates to some tens in the high and low frequency range and to obtain just a dull and affordable peak of one hundred iterates for the intermediate frequencies in the range from one to some kilo Hertz.

### 8.3. Assessing the asymptotically linear behaviour of FAIME

This section goal is testing the asymptotically linear behaviour that is achieved thanks to the new formulation based on the factorization of the inductance matrix for the frequency range typical of application of power electronics and inductive sensors (from statics to a few MHz). In addition to this, the performance of EFIE system solution when ACA is directly applied to  $\mathbb{K}$  matrix in place of its factorized version presented in this paper is compared to FAIME implementation in which FMM is used to get rid of the bottlenecks caused by being  $\mathbb{K}_M$  a dense matrix. Benefits and observations on this last point are exposed.

#### 8.3.1. Computational time scaling for a solid sphere

The asymptotically linear behaviour of FAIME is distinctly depicted in Fig. 17. The same result can be obtained if in place of the total computational time the Peak Memory Usage (PMU) is put in the ordinate axis.

This plot justifies the impact of the use of FMM in addition to the factorized expression of  $\mathbb{K}_M$  and validates the correctness of the code structure thus eliminating the otherwise quadratic scaling of time and memory occupation typical of all EFIE formulations. In other words, it is possible to state that FAIME exhibits a better asymptotic

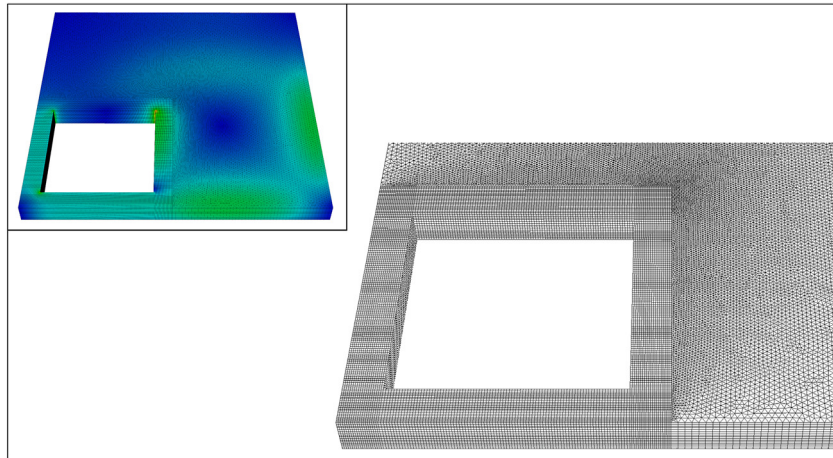


**Fig. 16.** Left-bottom corner of TEAM 7 mesh made of mixed hexahedra and triangular prisms. In the inset, for this mesh,  $\text{Real}(j)$  colour map at  $f = 50.0$  Hz is shown as a comparison to the one previously obtained in Fig. 12. (For interpretation of the references to colour in this figure legend, the reader is referred to the web version of this article.)

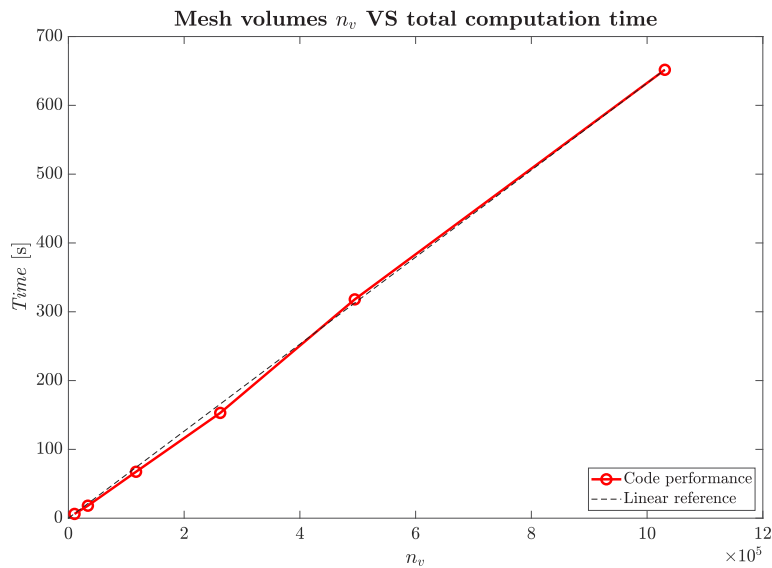


**Fig. 17.** Mesh elements and total computational time comparison.

computational complexity than FEM codes based on direct solvers like PARDISO (iterative solvers usually converge very slowly for eddy current problems formulated with FEM). In the following section, we also show that the same results cannot be obtained when algebraic compression techniques are directly applied to the whole  $\mathbb{K}$ .

### 8.3.2. Overall performance comparison with state-of-the-art

Table 3 relates the performance of the solution of EFIE when afforded with three different approaches: the standard solution of (48) where  $\mathbb{K}$  is computed and stored as a fully populated complex matrix (*Standard EFIE* in the table header), the algebraic compression of the whole  $\mathbb{K}$  entries by means of HLIBpro library [69] (*HLIBpro*

**Table 3**

Performance comparison in the Windows Server between state-of-the-art approaches and this paper code. Symmetry of the mass matrices is exploited in all the approaches.

	Standard EFIE	ACA/HLIBpro	FAIME
Matrices allocated memory [GB]	8,141	–	0.883
Non-zero entries stored	$1.0 \cdot 10^{12}$	–	$95 \cdot 10^6$
Tot. time	–	>24 h	649 s
PMU [GB]	–	–	13.5

**Table 4**

Mesh data and calculation time in the Windows Server for the conducting plate with seven holes.

Frequency [Hz]	$V$	$N_{dofs}$	Iterates	Assembly [s]	Solve [s]	Tot. time [s]
50.0	290,246	528,093	19	265.8	38.8	312.6

in the table header). These two approaches are regarded as state-of-the-art techniques. The third missing term of the comparison naturally is the novel FAIME approach presented in this paper (*FAIME* in the table).

In the proposed example, the considered configuration is the solid sphere problem at  $f = 50$  Hz,  $B_z = 1.0$  mT, in which the conductor is meshed with  $V = 1,030,656$  tetrahedra with corresponding 1,008,768 DoFs.

From a comparison of the data two main considerations can be done: the first, the trivial one, is that the standard approach is not suitable to deal with such a problem because of memory and time requirements that are anyhow prohibitive for a practical use of the code. The second aspect to be highlighted is that, even if HLIBpro might succeed in reducing and limiting the memory occupation, the same cannot be said for the computation time that still dramatically impacts into the overall performance making also this method not considerable to solve problems with a large number of unknowns. Differently, FAIME approach is effective in both squeezing the memory occupation and in drastically reducing the computation time too thus rendering this novel approach very promising for a wide range of practical problems.

For the sake of precision, it is here remarked that, in virtue of FAIME effectiveness in eliminating EFIE bottlenecks, the same problem has been also solved with FAIME approach in the Windows Laptop (16 GB of RAM), scoring a total computation time of 1,220 s of which 788.5 s for the matrices assembly. It can be deduced that the gap with respect to the computation time of the Windows Server is mainly due to the parallel implementation of FMM3D library and MKL PARDISO solver (4 vs 32 cores) used to factorize the preconditioner  $\mathbb{K}_R$  applied to solve the problem.

#### 8.4. A prismatic mesh of a plate with seven holes and a printed circuit board coil

To conclude the numerical results section, it is proposed in Fig. 18 the solution of the same problem considered by the authors in [70] whose results will be regarded as reference values for the present test. This last benchmark introduces two peculiar aspects not faced yet in the previous cases: the presence of a wider number of holes and thus of cohomology generators and the discretization of the conductor by means of triangular prismatic elements. The computed ohmic losses in the discrete grid are  $P_{diss} = 0.891$  mW that perfectly matches the values in [70]. Other aspects of the simulation performance are reported in Table 4.

Finally, in Fig. 19, a colour map of the real part of the current density field in a PCB coil fed by a sinusoidal voltage at 5 MHz is shown. The coil is composed by 8 copper turns and the outer turns have a radius of 20 mm. The copper section is  $0.2 \text{ mm} \times 35 \text{ }\mu\text{m}$ . The mesh used consists of 514,285 tetrahedra that yields 416,049 unknowns. The total simulation time is 242 s.

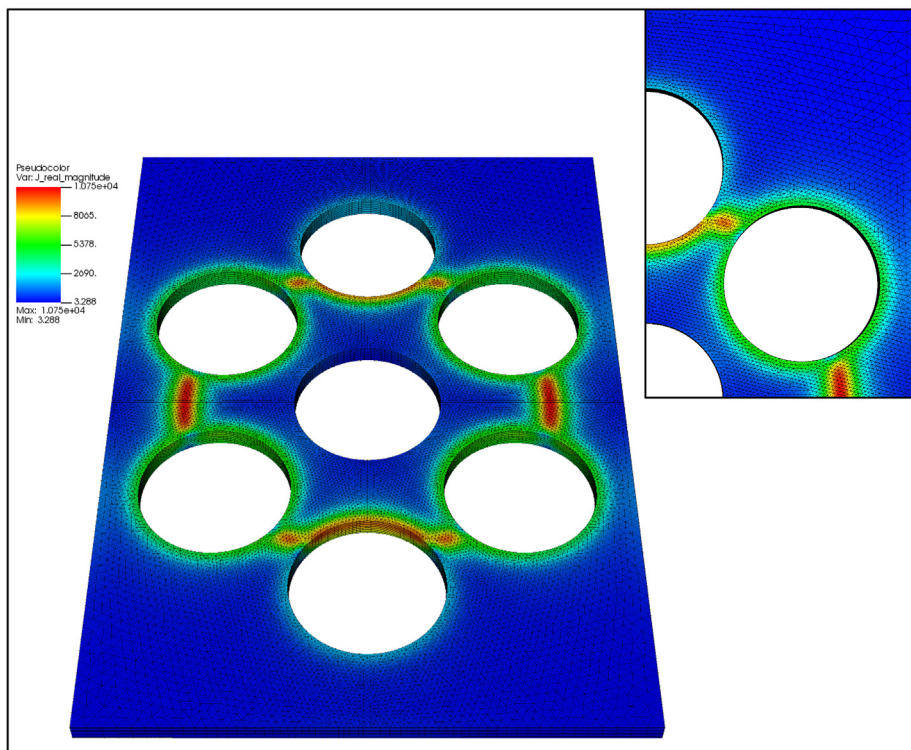


**Fig. 18.** Main picture: colour map of the real part of the current density field in the conducting plate with seven holes. Inset: a detail of the triangular faces of the prisms forming the mesh are depicted in one fourth of the original mesh. (For interpretation of the references to colour in this figure legend, the reader is referred to the web version of this article.)

## 9. Conclusion

Starting from the classical EFIE in the magneto-quasistatic limit, a novel compatible volume integral method to solve the eddy current problem has been introduced. The method roots on volume uniform basis functions, which provide the rational for taming the two main weaknesses of integral formulations. On one hand, the computation of the elements of the system matrix is improved with respect to speed and implementation simplicity. On the other hand, a novel factorization of the inductance matrix is introduced. This factorization induces a ground-breaking speedup of various orders of magnitude with respect to the state-of-the-art solutions (in particular, a popular ACA library) thanks to the use of fast summation techniques, like the Fast Multipole Method, to perform the matrix–vector product. Moreover, in our framework, one can use any off-the-shelf libraries developed for fast charge summation.

It is clear that all the techniques introduced in this paper for tetrahedra and general polyhedra can be readily adapted to triangles and general polygons. To deal with electrodes, magnetic materials and full Maxwell problems are the topics currently under investigation. In particular, the proposed basis functions and factorization can be universally applicable to any generalized mass matrices arising with any integral method or boundary element method.

## Declaration of competing interest

The authors declare the following financial interests/personal relationships which may be considered as potential competing interests: Mauro Passarotto, Silvano Pitassi and Ruben Specogna have deposited the Italian patent 102021000015602 filed on June 15, 2021 (patent pending).

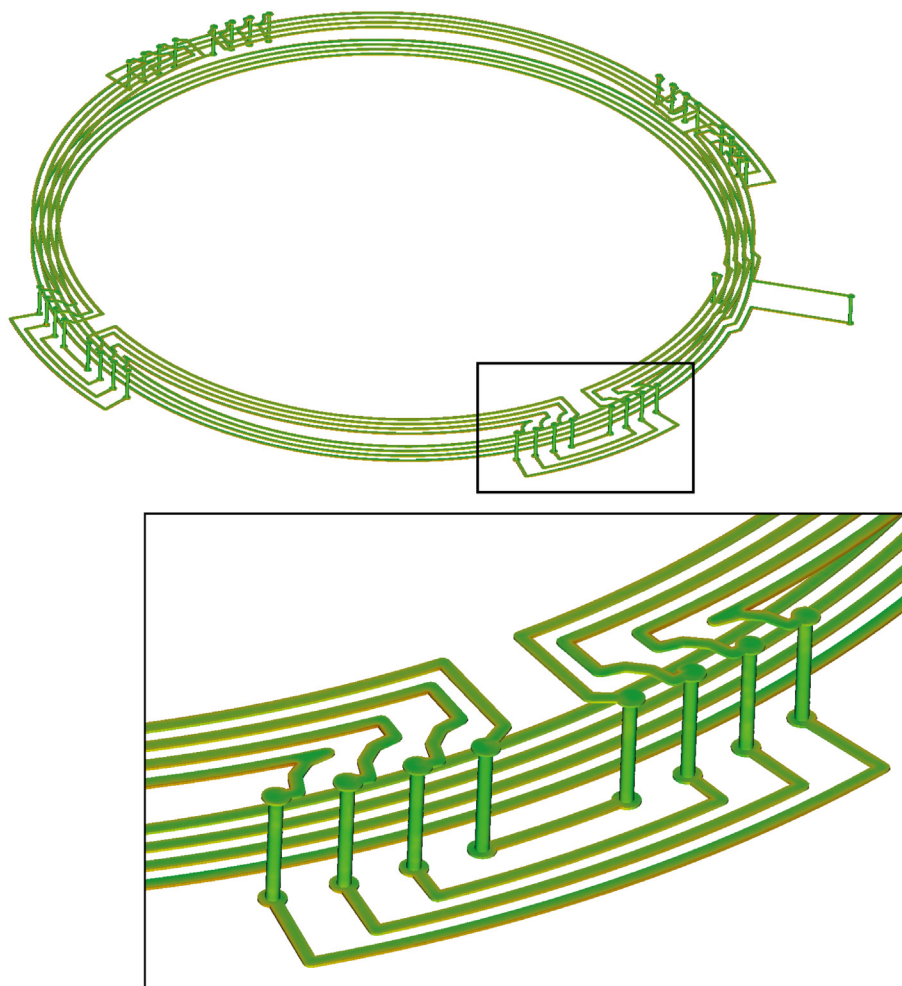


**Fig. 19.** Main picture: colour map of the real part of the current density field in a PCB coil. Inset: zoom of current density distribution. (For interpretation of the references to colour in this figure legend, the reader is referred to the web version of this article.)

## References

- [1] J. Maxwell, *A Treatise on Electricity and Magnetism*, Clarendon Press, Oxford, UK, 1891.
- [2] A. Rodriguez, A. Valli, *Eddy Current Approximation Of Maxwell Equations: Theory, Algorithms And Applications*, in: MS&A, Springer Milan, 2010.
- [3] I. Kovacevic-Badstuebner, D. Romano, G. Antonini, J. Ekman, U. Grossner, Broadband circuit-oriented electromagnetic modeling for power electronics: 3-D PEEC solver vs. RLCG-solver, *Energies* 14 (10) (2021) 2835, <http://dx.doi.org/10.3390/en14102835>.
- [4] R. Torchio, F. Lucchini, J.-L. Schanen, O. Chadebec, G. Meunier, FFT-PEEC: A fast tool from CAD to power electronics simulations, *IEEE Trans. Power Electron.* (2021) 1, <http://dx.doi.org/10.1109/tpel.2021.3092431>.
- [5] R. Torchio, V. Cirimele, P. Alotto, F. Freschi, Modelling of road-embedded transmitting coils for wireless power transfer, *Comput. Electr. Eng.* 88 (2020) 106850, <http://dx.doi.org/10.1016/j.compeleceng.2020.106850>.
- [6] Z. Guo, G. Wang, An edge-based smoothed finite element method for the assessment of human exposure to extremely low frequency electric fields, *Comput. Methods Appl. Mech. Eng.* 370 (2020) 113280, <http://dx.doi.org/10.1016/j.cma.2020.113280>.
- [7] J. Chovan, C. Geuzaine, M. Slodička, A- $\phi$  formulation of a mathematical model for the induction hardening process with a nonlinear law for the magnetic field, *Comput. Methods Appl. Mech. Eng.* 321 (2017) 294–315, <http://dx.doi.org/10.1016/j.cma.2017.03.045>.
- [8] A. Alonso Rodríguez, E. Bertolazzi, R. Ghiloni, A. Valli, Finite element simulation of eddy current problems using magnetic scalar potentials, *J. Comput. Phys.* 294 (2015) 503–523, <http://dx.doi.org/10.1016/j.jcp.2015.03.060>.
- [9] J. Dölz, S. Kurz, S. Schöps, F. Wolf, A numerical comparison of an isogeometric and a parametric higher order Raviart–Thomas approach to the electric field integral equation, *IEEE Trans. Antennas Propag.* 68 (1) (2020) 593–597, <http://dx.doi.org/10.1109/TAP.2019.2935778>.

- [10] A. Simona, L. Bonaventura, C. de Falco, S. Schöps, IsoGeometric approximations for electromagnetic problems in axisymmetric domains, *Comput. Methods Appl. Mech. Eng.* 369 (2020) 113211, <http://dx.doi.org/10.1016/j.cma.2020.113211>.
- [11] L. Camargo, B. López-Rodríguez, M. Osorio, M. Solano, An HDG method for Maxwell's equations in heterogeneous media, *Comput. Methods Appl. Mech. Eng.* 368 (2020) 113178, <http://dx.doi.org/10.1016/j.cma.2020.113178>.
- [12] K. Lipnikov, G. Manzini, F. Brezzi, A. Buffa, The mimetic finite difference method for the 3D magnetostatic field problems on polyhedral meshes, *J. Comput. Phys.* 230 (2) (2011) 305–328, <http://dx.doi.org/10.1016/j.jcp.2010.09.007>.
- [13] L. Beirão da Veiga, F. Brezzi, F. Dassi, L. Marini, A. Russo, Lowest order virtual element approximation of magnetostatic problems, *Comput. Methods Appl. Mech. Eng.* 332 (2018) 343–362, <http://dx.doi.org/10.1016/j.cma.2017.12.028>.
- [14] L. Beirão da Veiga, F. Dassi, G. Manzini, L. Mascotto, Virtual elements for Maxwell's equations, *Comput. Math. Appl.* (2021) <http://dx.doi.org/10.1016/j.camwa.2021.08.019>.
- [15] D.A. Di Pietro, J. Droniou, An arbitrary-order method for magnetostatics on polyhedral meshes based on a discrete de Rham sequence, *J. Comput. Phys.* 429 (2021) 109991, <http://dx.doi.org/10.1016/j.jcp.2020.109991>.
- [16] A. Ruehli, Equivalent circuit models for three-dimensional multiconductor systems, *IEEE Trans. Microwave Theory Tech.* 22 (3) (1974) 216–221, <http://dx.doi.org/10.1109/TMTT.1974.1128204>.
- [17] M. Kamon, M.J. Tsuk, J.K. White, FastHenry: a multipole-accelerated 3-D inductance extraction program, *IEEE Trans. Microwave Theory Tech.* 42 (9) (1994) 1750–1758, <http://dx.doi.org/10.1109/22.310584>.
- [18] A. Ruehli, G. Antonini, L. Jiang, *Circuit Oriented Electromagnetic Modeling Using The PEEC Techniques*, in: Wiley - IEEE, Wiley, 2017.
- [19] L. Lombardi, D. Romano, G. Antonini, Accurate and efficient low-frequency solution of partial element equivalent circuit models, *IEEE Trans. Electromagn. Compat.* 59 (5) (2017) 1514–1522, <http://dx.doi.org/10.1109/TEMC.2017.2651022>.
- [20] R. Torchio, A volume PEEC formulation based on the cell method for electromagnetic problems from low to high frequency, *IEEE Trans. Antennas Propag.* 67 (12) (2019) 7452–7465, <http://dx.doi.org/10.1109/TAP.2019.2927789>.
- [21] R. Albanese, G. Rubinacci, Integral formulation for 3D eddy-current computation using edge elements, *IEE Proc. A* 135 (7) (1988) 457–462, <http://dx.doi.org/10.1049/ip-a-1.1988.0072>.
- [22] R. Albanese, G. Rubinacci, Finite element methods for the solution of 3D eddy current problems, *Adv. Imag. Electr. Phys.* (1997) [http://dx.doi.org/10.1016/S1076-5670\(08\)70121-6](http://dx.doi.org/10.1016/S1076-5670(08)70121-6).
- [23] C. Forestiere, G. Miano, G. Rubinacci, A. Tamburrino, R. Tricarico, S. Ventre, Volume integral formulation for the calculation of material independent modes of dielectric scatterers, *IEEE Trans. Antennas Propag.* 66 (5) (2018) 2505–2514, <http://dx.doi.org/10.1109/TAP.2018.2816604>.
- [24] D. Voltolina, R. Torchio, P. Bettini, R. Specogna, P. Alotto, Optimized cycle basis in volume integral formulations for large scale eddy-current problems, *Comput. Phys. Comm.* 265 (2021) 108004, <http://dx.doi.org/10.1016/j.cpc.2021.108004>.
- [25] M. Bebendorf, S. Rjasanow, Adaptive low-rank approximation of collocation matrices, *Computing* 70 (1) (2003) 1–24, <http://dx.doi.org/10.1007/s00607-002-1469-6>.
- [26] K. Zhao, M.N. Vouvakis, J.-F. Lee, The adaptive cross approximation algorithm for accelerated method of moments computations of EMC problems, *IEEE Trans. Electromagn. Compat.* 47 (4) (2005) 763–773, <http://dx.doi.org/10.1109/TEMC.2005.857898>.
- [27] S. Kurz, O. Rain, S. Rjasanow, The adaptive cross-approximation technique for the 3D boundary-element method, *IEEE Trans. Magn.* 38 (2) (2002) 421–424, <http://dx.doi.org/10.1109/20.996112>.
- [28] A.C. Yucel, I.P. Georgakis, A.G. Polimeridis, H. Bağcı, J.K. White, VoxHenry: FFT-accelerated inductance extraction for voxelized geometries, *IEEE Trans. Microwave Theory Tech.* 66 (4) (2018) 1723–1735, <http://dx.doi.org/10.1109/TMTT.2017.2785842>.
- [29] M. Li, M.A. Francavilla, F. Vipiana, G. Vecchi, R. Chen, Nested equivalent source approximation for the modeling of multiscale structures, *IEEE Trans. Antennas Propag.* 62 (7) (2014) 3664–3678, <http://dx.doi.org/10.1109/TAP.2014.2321139>.
- [30] M. Li, M.A. Francavilla, R. Chen, G. Vecchi, Nested equivalent source approximation for the modeling of penetrable bodies, *IEEE Trans. Antennas Propag.* 65 (2) (2017) 954–959, <http://dx.doi.org/10.1109/TAP.2016.2632518>.
- [31] S. Pitassi, F. Trevisan, R. Specogna, Explicit geometric construction of sparse inverse mass matrices for arbitrary tetrahedral grids, *Comput. Methods Appl. Mech. Eng.* 377 (2021) 113699, <http://dx.doi.org/10.1016/j.cma.2021.113699>.
- [32] FMM3D, 2020, <https://www.simonsfoundation.org/flatiron/software/>. (Accessed June 2020).
- [33] *Mathematical Society of Japan, Kiyosi Ito (Eds.), Encyclopedic Dictionary of Mathematics*, MIT Press, Cambridge, MA, 1987.
- [34] A. Bossavit, On the numerical analysis of eddy-current problems, *Comput. Methods Appl. Mech. Eng.* 27 (3) (1981) 303–318, [http://dx.doi.org/10.1016/0045-7825\(81\)90135-3](http://dx.doi.org/10.1016/0045-7825(81)90135-3).
- [35] A. Bossavit, Whitney forms: a class of finite elements for three-dimensional computations in electromagnetism, *IEE Proc. A* 135 (8) (1988) 493–500, <http://dx.doi.org/10.1049/ip-a-1.1988.0077>.
- [36] P.A. Raviart, J.M. Thomas, A mixed finite element method for 2-nd order elliptic problems, in: *Lecture Notes In Mathematics*, Springer Berlin Heidelberg, 1977, pp. 292–315, <http://dx.doi.org/10.1007/bfb0064470>.
- [37] S. Rao, D. Wilton, A. Glisson, Electromagnetic scattering by surfaces of arbitrary shape, *IEEE Trans. Antennas Propag.* 30 (3) (1982) 409–418, <http://dx.doi.org/10.1109/TAP.1982.1142818>.
- [38] D. Schaubert, D. Wilton, A. Glisson, A tetrahedral modeling method for electromagnetic scattering by arbitrarily shaped inhomogeneous dielectric bodies, *IEEE Trans. Antennas Propag.* 32 (1) (1984) 77–85, <http://dx.doi.org/10.1109/TAP.1984.1143193>.
- [39] S.M. Rao, D.R. Wilton, A.W. Glisson, RWG functions: Evolution and progress, in: *Wiley Encyclopedia Of Electrical And Electronics Engineering*, 2016, pp. 1–13, <http://dx.doi.org/10.1002/047134608X.W8308>.
- [40] J.R. Munkres, *Elements Of Algebraic Topology*, Westview Press, 1993, <http://dx.doi.org/10.1201/9780429493911>.
- [41] E. Tonti, *The Mathematical Structure Of Classical And Relativistic Physics: A General Classification Diagram*, in: *Modeling and Simulation in Science, Engineering and Technology*, Springer New York, 2013.

- [42] A. Bossavit, 'Generalized finite differences' in computational electromagnetics, *Prog. Electromagn. Res.* 32 (2001) 45–64, <http://dx.doi.org/10.2528/PIER00080102>.
- [43] L. Codecasa, R. Specogna, F. Trevisan, A new set of basis functions for the discrete geometric approach, *J. Comput. Phys.* 229 (19) (2010) 7401–7410, <http://dx.doi.org/10.1016/j.jcp.2010.06.023>.
- [44] S. Pitassi, R. Ghiloni, F. Trevisan, R. Specogna, The role of the dual grid in low-order compatible numerical schemes on general meshes, *J. Comput. Phys.* 436 (2021) 110285, <http://dx.doi.org/10.1016/j.jcp.2021.110285>.
- [45] R. Albanese, G. Miano, G. Rubinacci, R. Martone, A  $t$  formulation for 3D finite element eddy current computation, *IEEE Trans. Magn.* 21 (6) (1985) 2299–2302, <http://dx.doi.org/10.1109/TMAG.1985.1064186>.
- [46] J.C. Nedelec, Mixed finite elements in  $\mathbb{R}^3$ , *Numer. Math.* 35 (3) (1980) 315–341, <http://dx.doi.org/10.1007/BF01396415>.
- [47] G. Rubinacci, A. Tamburrino, Automatic treatment of Multiply Connected Regions in integral formulations, *IEEE Trans. Magn.* 46 (8) (2010) 2791–2794, <http://dx.doi.org/10.1109/TMAG.2010.2043722>.
- [48] H.A. Haus, J.R. Melcher, *Basic Circuit Theory*, MacGraw-Hill, New York, 1969.
- [49] N. Balabanian, *Electrical Network Theory*, Wiley, 1969.
- [50] J. Siau, G. Meunier, O. Chadebec, J. Guichon, R. Perrin-Bit, Volume integral formulation using face elements for electromagnetic problem considering conductors and dielectrics, *IEEE Trans. Electromagn. Compat.* 58 (5) (2016) 1587–1594, <http://dx.doi.org/10.1109/TEMC.2016.2559801>.
- [51] P. Bettini, M. Passarotto, R. Specogna, A volume integral formulation for solving eddy current problems on polyhedral meshes, *IEEE Trans. Magn.* 53 (6) (2017) <http://dx.doi.org/10.1109/TMAG.2017.2663112>.
- [52] P. Dlotko, R. Specogna, Physics inspired algorithms for (co)homology computations of three-dimensional combinatorial manifolds with boundary, *Comput. Phys. Comm.* 184 (10) (2013) 2257–2266, <http://dx.doi.org/10.1016/j.cpc.2013.05.006>.
- [53] P. Bamberg, S. Sternberg, *A Course In Mathematics For Students Of Physics*, Cambridge University Press, Cambridge, UK, 1988, <http://dx.doi.org/10.1017/CBO9781139171670>.
- [54] M. Marrone, Properties of constitutive matrices for electrostatic and magnetostatic problems, *IEEE Trans. Magn.* 40 (3) (2004) 1516–1520, <http://dx.doi.org/10.1109/TMAG.2004.827175>.
- [55] P. Dular, J. Hody, A. Nicolet, A. Genon, W. Legros, Mixed finite elements associated with a collection of tetrahedra, hexahedra and prisms, *IEEE Trans. Magn.* 30 (5) (1994) 2980–2983, <http://dx.doi.org/10.1109/20.312563>.
- [56] F. Brezzi, K. Lipnikov, V. Simoncini, A Family of mimetic finite difference methods on polygonal and polyhedral meshes, *Math. Models Methods Appl. Sci.* 15 (10) (2005) 1533–1551, <http://dx.doi.org/10.1142/S0218202505000832>.
- [57] J. Bonelle, D.A.D. Pietro, A. Ern, Low-order reconstruction operators on polyhedral meshes: application to compatible discrete operator schemes, *Comput. Aided Geom. Design* 35–36 (2015) 27–41, <http://dx.doi.org/10.1016/j.cagd.2015.03.015>.
- [58] M. Passarotto, R. Specogna, F. Trevisan, Novel geometrically defined mass matrices for tetrahedral meshes, *IEEE Trans. Magn.* 55 (6) (2019) <http://dx.doi.org/10.1109/TMAG.2019.2893692>.
- [59] S. Jarvenpaa, M. Taskinen, P. Ylä-Oijala, Singularity extraction technique for integral equation methods with higher order basis functions on plane triangles and tetrahedra, *Int. J. Numer. Methods Eng.* 58 (8) (2003) 1149–1165, <http://dx.doi.org/10.1002/nme.810>.
- [60] S. Jarvenpaa, M. Taskinen, P. Ylä-Oijala, Singularity subtraction technique for high-order polynomial vector basis functions on planar triangles, *IEEE Trans. Antennas Propag.* 54 (1) (2006) 42–49, <http://dx.doi.org/10.1109/TAP.2005.861556>.
- [61] D. Wilton, S. Rao, A. Glisson, D. Schaubert, O. Al-Bundak, C. Butler, Potential integrals for uniform and linear source distributions on polygonal and polyhedral domains, *IEEE Trans. Antennas Propag.* 32 (3) (1984) 276–281, <http://dx.doi.org/10.1109/TAP.1984.1143304>.
- [62] R.A. Werner, D.J. Scheeres, Exterior gravitation of a polyhedron derived and compared with harmonic and mascon gravitation representations of asteroid 4769 Castalia, *Celest. Mech. Dyn. Astron.* 65 (3) (1997) <http://dx.doi.org/10.1007/bf00053511>.
- [63] R.A. Werner, D.J. Scheeres, *Mutual Potential of Homogeneous Polyhedra*, Vol. 91, No. 3–4, Springer Science and Business Media LLC, 2005, pp. 337–349, <http://dx.doi.org/10.1007/s10569-004-4621-0>.
- [64] S. Bao, D. Wang, Y. Mo, S. Hu, J. Gu, W. Tang, Fully analytical evaluation of singular integrals with RWG and rooftop basis functions, *IEEE J. Multiscale Multiphys. Comput. Tech.* 5 (2020) 217–226, <http://dx.doi.org/10.1109/JMMCT.2020.3029064>.
- [65] Y. Saad, M. Schultz, GMRES: a generalized minimal residual algorithm for solving nonsymmetric linear systems, *SIAM J. Sci. Stat. Comput.* 7 (3) (1986) 856–869, <http://dx.doi.org/10.1137/0907058>.
- [66] G. Rubinacci, A. Tamburrino, S. Ventre, F. Villone, A fast 3-D multipole method for eddy-current computation, *IEEE Trans. Magn.* 40 (2) (2004) 1290–1293, <http://dx.doi.org/10.1109/TMAG.2004.824585>.
- [67] M. Nayfeh, *Electricity And Magnetism*, Dover Publications, Inc, Mineola, New York, 2015.
- [68] K. Fujiwara, T. Nakata, Results for benchmark problem 7 (asymmetrical conductor with a hole), *COMPEL Int. J. Comput. Math. Electr. Electr. Eng.* 9 (3) (1990) 137–154, <http://dx.doi.org/10.1108/eb010071>.
- [69] HLIBpro, 2020, <https://www.hlibpro.com/>. (Accessed May 2020).
- [70] M. Passarotto, D. Klis, O. Rain, R. Specogna, Mirror symmetry in integral formulations for eddy currents, *IEEE Trans. Magn.* 57 (6) (2021) <http://dx.doi.org/10.1109/TMAG.2021.3065253>.